Silver Nanowire Transparent Conductors for Quantum Dot Photovoltaics

Natasha Hjerrild

St. Edmund Hall

A thesis submitted for the degree of

MSc in Materials

University of Oxford

ABSTRACT

This thesis studies the application of silver nanowire transparent conductors in PbS quantum dot photovoltaics.

Silver nanowires were synthesized using a colloidal method and characterized using scanning electron microscopy. Nanowires were deposited on glass substrates by a stamp transfer process to generate a low density continuous network of conductive nanowires. This resulted in a highly conductive and transparent film appropriate for optoelectronic applications. Nanowire synthesis, deposition, and processing were optimised to produce transparent conductors suitable for thin film photovoltaics.

These nanowire films were used to fabricate lead sulphide (PbS) colloidal quantum dot solar cells. In this structure, p-type PbS quantum dots form a junction with a n-type ZnO nanoparticle layer. A variety of fabrication and processing treatments were developed in order to reduce short-circuiting of devices and to enhance cell performance. Moderate nanowire density, improved ZnO adherence, slight device aging, and increased PbS film thickness proved to result in the highest quality devices. The champion device developed in this thesis achieved a power conversion efficiency of 2.2%.

ACKNOWLEDGEMENTS

I would like to thank Dr. Andrew Watt for his advice, encouragement and for giving me so much freedom with my project. He taught me to question what I know, tirelessly helped me with my research outside normal work hours, and provided hot chocolate after very rainy bicycle rides to lab. I thank Dr. Jamie Warner for his guidance with nanowire synthesis enhancement and project management. I thank Dr. John Topping for his integrating sphere expertise and for keeping every day in lab exciting. I thank Dr. Peter Kovacik for his assistance with MicroXAM and his help with film topographical issues.

I would like to thank Chi (Darren) Neo for providing the quantum dots and for sharing his quantum dot device knowledge. From half marathons to our collaborated research, I couldn’t have asked for a more encouraging and enthusiastic lab partner and friend.

Thanks to Cheng Cheng for his help with cell fabrication and for his assistance with device issues. Thanks to Assia Kasdi for sharing her chemistry knowledge of nanowire synthesis and processing. Thanks to Chris Cattley for his help with lab issues and for generally maintaining sanity in the group. Thanks to Camden Ford for his colourful humour and friendship. Thanks to Inji Yeom for sharing my love for doing experimental work to Disney soundtracks. Thanks to Jenna Holder and Laura Drossler for making the lab a fun, friendly place to work.

Most of all, I would like to thank Grandma, Grandpa, Mom, Dad and Benny Boy. Your love and support made this thesis possible.

DECLARATION OF ORIGINALITY

This thesis is an account of work carried out by the author in the Department of Materials, the University of Oxford under the supervision of Dr. Andrew Watt and Dr. Jamie Warner. Any work of others that has been drawn upon is duly acknowledged in the text, and a list of references is presented at the thesis. No part of this thesis has been submitted towards the completion of another degree at the University of Oxford or elsewhere.

TABLE OF CONTENTS

LIST OF ABBREVIATIONS

Ag NW	Silver nanowire
BHJ	Bulk heterojunction
E_o	Internal electric field
E_g	Energy band gap
FF	Fill factor
ITO	Indium tin oxide
J_{sc}	Short circuit current density
J_o	Leakage current density
L_{avg}	Average length of nanowire
NW	Nanowire
PbS	Lead Sulphide
PCE	Power conversion efficiency
PEDOT: PSS	Poly(3,4-ethylenedioxythiophene) poly(styrenesulfonate)
PV	Photovoltaic
PVP	Poly(vinyl pyrrolidone)
QD	Quantum dot
R_{series}	Series resistance
R_{sheet}	Sheet resistance
R_{shunt}	Shunt resistance
TC	Transparent conductor
V_{oc}	Open-circuit voltage

CHAPTER 1 - INTRODUCTION

1.1 Motivation for Solution-Processed Solar Cells

Since the fabrication of the first practical silicon solar cell in 1954,[1] photovoltaic (PV) devices have been widely regarded as a completely renewable energy source that could end reliance upon burning fossil fuels for electricity generation.[2] The amount of energy continuously offered by solar irradiation, 1.2×10^5 TW globally, dwarfs the global average power use of ~13TW and is offered with far greater availability and abundance than any other power source, renewable and non-renewable alike.[3] Furthermore, because the replacement of all coal and gas-fired power plants with central PV installations can reduce greenhouse gas emissions between 89-98%, PV offers a promising means of minimizing human impacts on climate change.[4]

Dramatic price reductions of PV modules have caused solar installations to rise steadily in recent years, with a 54% increase of deployment in 2011 from 2010.[5] Currently, over 50% of the cost for standard crystalline silicon solar cells is attributed to silicon wafer production.[6] Among other factors, this expense arises from the cost of high purity silicon ingots, slow wafer throughput, and high materials loss due to wafer fracture during sawing.[7]

Roll-to-roll processing is an alternative method of PV fabrication based on rapid deposition of a photosensitive ink on a flexible substrate. This high-throughput, low-temperature manufacturing process shows great promise for drastically reducing the cost of solar cells and simultaneously providing the benefits of light-weight, flexible

PV modules which are less cumbersome and more adaptable than standard, rigid PV modules.[8] However, one major difficulty to the commercialization of this roll-to-roll photovoltaic technology is the poor availability of flexible transparent conductors needed to extract the photocurrent.[9]

Recent developments in nanocrystal synthesis methods have developed semiconductor quantum dot and conductive nanowire inks which can be deposited as the photosensitive and transparent conductor layer, respectively.[10,11] The combination of these two technologies is central to the aims of this thesis.

1.2 Aims for this Thesis

The purpose of this study is to produce a low-temperature, solution-processed solar cell using a silver nanowire film as the transparent conductor and lead sulphide quantum dots as the absorber layer. The objectives to achieve this goal are as follows:

1. Reproducibly synthesize quality silver nanowires.
2. Optimise silver nanowire deposition in order to maximize optical and electrical properties of the films.
3. Fabricate functional PbS quantum dot solar cells using the optimised nanowire film.
4. Upon fabrication of functioning solar cells, identify and understand sources of weakness within the device and establish routes to resolve these issues for improved device performance.

Background information is provided for these aims, beginning with the desired characteristics of a transparent conductor and how these properties impact solar cell performance.

CHAPTER 2 – BACKGROUND INFORMATION

2.1 Transparent Conductors

2.1.1 WHAT IS A TRANSPARENT CONDUCTOR?

Transparent conductors (TCs) are materials which typically transmit >80% of the visible spectrum and offer sheet resistances (R_{sheet}) less than 20 Ω/□. TCs are a critical component in televisions, computers, cell phones, tablets, and photovoltaic (PV) devices.[12] Because of this, the TC market is expected to grow to $6.9 billion by 2016.[13]

Desired TC properties vary according to application. For example, optical haze is devastating to applications of TCs in most electronic displays, but can enhance high efficiency photovoltaics due to the extended optical path length which increases the likelihood of photon absorption by the photosensitive material.[14] Regardless, across all devices, the two most important parameters are the TC sheet resistance and optical transparency.[12]

2.1.2 QUALITY MEASUREMENT OF TRANSPARENT CONDUCTORS

2.1.2.1 Sheet Resistance

The electrical conductivity of a material is dictated by the electron mobility within the conductive layer. Electron scattering, caused by electron interaction with phonons, grain boundaries, or dopants, can greatly reduce electron mobility, and should be minimized for optimal TC performance.[12]

Electrical conductivity requirements differ according to application of TCs, although solar cells require a TC sheet resistance (R_{sheet}) on the scale of ~10 Ω/sq.[9] R_{sheet} can be calculated by Equation 1 where ρ*(t)* is the film resistivity, which is dictated by film thickness, *t*, due to microstructural variations and edge effects of thin films.[12]

$$R_{Sheet} = \frac{\rho(t)}{t} \qquad \textbf{(1)}$$

2.1.2.2 Transmittance

For TC reflectance and absorption coefficient values at a given wavelength, respectively R_λ and α_λ, transmittance of an unsupported film at any wavelength can be calculated using Equation 2.[15]

$$T_\lambda = (1 - R_\lambda)^2 \exp(-\alpha_\lambda t) \qquad \textbf{(2)}$$

A low refractive index anti-reflective coating can reduce R_λ to increase the transmittance of the film.[9] Material transmittance can be separated into specular and diffusive transmittance. Specular transmittance is the transmittance of photons along the angle of incident light, whereas diffusive transmittance accounts for optical scattering within the film which may alter the path of the photon.[14] This diffusive transmittance can enhance solar cell performance due to an increased photonic path length.[16]

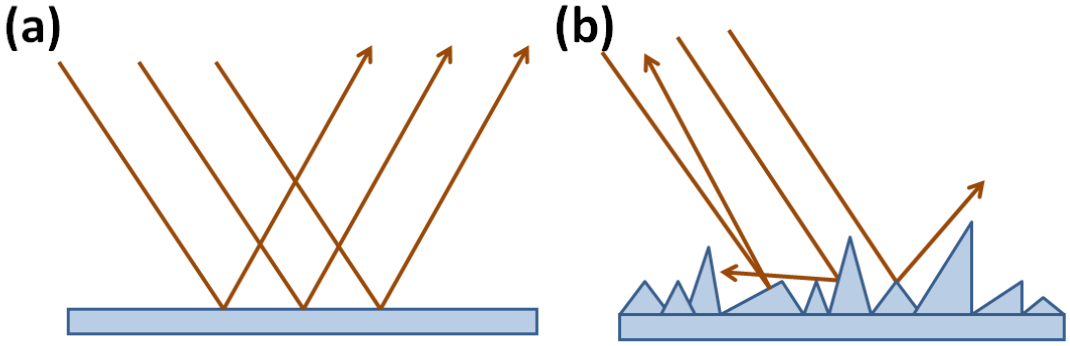

Figure 2.1: (a) Specular reflection from a smooth film, along the angle of incidence, and (b) diffuse reflection caused by high surface roughness.

Specular and diffuse behaviour also applies to reflectance of films, shown in Figure 2.1. Specular behaviour is standard of smooth film, where an axis normal to the plane of the film is consistent across the TC. Diffuse reflection, otherwise known as scattering, is common for rough films, as the perpendicular axis varies widely throughout the film.[17]

2.1.2.2 Other TC Properties

Transmittance and R_{sheet} values can be combined in a figure of merit to evaluate TC quality,

$$\frac{\sigma}{\alpha} = -[R_{sheet} \ln(T+R)]^{-1} \qquad \textbf{(3)}$$

where T and R are the averaged transmittance and reflectance across the visible spectrum of light, respectively. The larger the calculated value of this conductivity to absorption ratio, $\frac{\sigma}{\alpha}$, the better the TC will perform.[12]

Although not considered as crucial as transparency and electrical conductivity, other properties which prove to be helpful in the assessment of TC films are flexibility, physical, chemical and thermal durability, work function, film thickness, deposition temperature and technique, toxicity, film uniformity, and cost.[12] From a marketing viewpoint, this last TC property, cost, plays a crucial role in determining the future of the TC market.

2.1.3 MOTIVATION FOR ALTERNATIVE TRANSPARENT CONDUCTORS

2.1.3.1 ITO

Since the 1960s, tin-doped indium oxide (ITO) has been the most widely used TC in optoelectronic devices.[18] In addition to excellent electrical conductivity (~10 Ω/sq) [19] and high transparency (>90%), ITO offers good surface morphology, high reproducibility, and resistance to environmental degradation.[18]

Despite the many desirable characteristics of ITO, there are also many problems associated with ITO TCs. A critical shortage of indium, with some estimates claiming near-depletion of accessible indium resources as early as 2019,[20] has contributed to rising costs in recent years, with a 25% increase in the annual average price of indium from 2010 to 2011.[21] Poor mechanical flexibility and brittle morphology are additional drawbacks which prevent roll-to-roll deposition and restrict substrate applications.[9] These issues are good incentives to find competitive alternatives to ITO.

2.1.3.2 Other Alternatives

Alternative TCs vary from carbon nanotube networks, graphene, and thin metal films.[22] While graphene and carbon nanotubes can yield quality TCs, the expensive laser ablation and chemical vapour deposition growth processes are prohibitively expensive for large-scale TC fabrication.[23,24]

Metals boast high electronic conductivity at room temperature due to intrinsic high free-electron density. A very thin metal layer (a few 10s of nm) will appear transparent, regardless of the fact that bulk metals are typically highly reflective in the visible range.[24] However, electron scattering at the substrate surface and grain boundaries increases substantially for metal films less than 20 nm which leads to significantly greater R_{sheet} values.[25] The relatively low transmissivity, high materials cost, and expensive vacuum environments required for deposition decrease the viability of thin metal films as an alternative for ITO.[9] Despite the drawbacks of thin metal films, a deposited network of thin metal wires can increase transmissivity of the film and decrease the materials cost for the film without significantly decreasing the electrical conductivity of the TC. Furthermore, metal nanowires do not require expensive vacuum deposition.[26] The result of this concept is the nanowire TC.

2.1.4 SILVER NANOWIRE TRANSPARENT CONDUCTORS

Nanowires (NWs) are metal structures with diameters of 10s of nms and lengths up to 10s or 100s of μms.[27,28] Electrical conductivities along the length of NWs are similar to that of the bulk metal because high aspect ratio NWs have fewer grain boundaries and strained surfaces to promote electron scattering than smaller metal nanostructures. Therefore, a well-connected network of NWs will effectively transport charges and simultaneously increase light transmissivity compared to a thin metal film, due to unencumbered light penetration between NWs and forward photonic scattering caused by NWs.[26]

Because silver (Ag) has the highest electrical conductivity of any metal, it is a logical material choice for NW synthesis. Silver nanowires (Ag NWs) are typically >10μm in length and <100nm in diameter and provide an electrically conductive film when deposited as an interconnected NW network.[29] The quality of such an interconnected network can be assessed using percolation theory.

2.1.4.1 Percolation Theory

For an electrical current to travel across a NW TC, charge carriers move along the length of the NW at rates similar to that of bulk metal and can change direction of travel at junctions with other NWs. High connectivity between NWs is necessary in order to produce high electron mobility within the film. The connectivity of Ag NWs can be assessed using percolation theory, assuming the nanostructures are of aspect ratios >100. The sheet conductivity (σ_S) can be approximated,

$$\sigma_s \propto (N - N_c)^{\alpha} \qquad \textbf{(4)}$$

where N is the NW density measured in NW/area, N_C is the critical NW density at which the film becomes conductive, and α is the critical exponent that relates to the NW spatial geometry, ranging from 1.33 for 2D networks to 1.94 for 3D networks. Because NW networks are not perfectly 2-dimensional, causing some electron transport perpendicular to the plane of the film, experimental calculations of α values for NW networks are slightly greater than 1.33, ranging from 1.42 to 1.5.[30,22] Equation 5 evaluates the N_c value for a NW film with average NW length *l*.[22]

$$l\sqrt{\pi N_C} = 4.236 \qquad \textbf{(5)}$$

However, it should be noted that the broad application of this theory generates some sources of error. First, this theory is not specifically designed for any particular material, but instead is designed for general nanorod simulations, with some alterations for specific crystal structures. Because inherent electrical conductivity varies between materials, the R_{sheet} of NW films of different materials would also be impacted.[31] Additionally, this theory does not account for conductivity variance at nanorod junctions, which is an important factor to consider, as Ag NW films have been proven to be most resistive at junction sites.[14] Finally, this simulation relies solely on an average nanorod length. Thus, a very large distribution of NW lengths could significantly reduce the accuracy of the percolation theory.[31]

The percolation theory thus can be used to loosely determine the desired density of deposited NWs, although the length of the NWs is determined by the Ag NW synthesis process.

2.1.4.2 Silver Nanowire Synthesis

In this thesis, silver nanowires are produced by the polyol process, which requires a polyol to reduce metal salt precursors in the presence of a polymeric capping agent. For Ag NW synthesis, $AgNO_3$ is reduced by ethylene glycol (EG) in the presence of the polymeric capping agent poly(vinyl pyrrolidone) (PVP).[11]

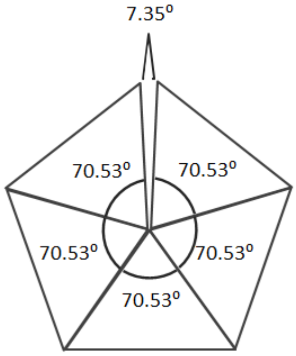

Figure 2.2: Decahedron formed by 5-fold twinning of silver tetrahedrons. The diameter remains relatively small since the 7.53^0 gap creates bond strain, which increases with increasing diameter.

Silver nuclei often combine by twin boundary defects in order to lower surface energy. The lowest free energy of silver nanostructures is achieved by a 5-fold twinned decahedron, shown in Figure 2.2, because it minimizes the number of strained bonds due to the relatively low 7.53^0 lattice mismatch.[11] The strain created by this angle mismatch is enhanced for NWs with larger radii, thus Ag atom attachment along the axis is favoured over increasing Ag NW diameters.[32] It has been found that this pentagonal structure formed by the twinned boundaries produces superior mechanical properties, such as a higher Young's modulus as well as a higher yield strength compared to bulk silver.[33]

Like all noble metals, silver crystallizes as a face-centred cubic crystal, giving rise to an inequality of site preference for PVP affixation between the {111} facets and the {100} faces during the formation of the nanostructures. The nanostructure produced is therefore dictated by the relative growth rates in these directions.[34] NWs are produced when PVP coats the {100} side facets of a decahedron nuclei (Figure 2.3a), allowing for Ag atoms to attach to the {111} end facets (Figure 2.3b).[11] The difference in attraction energy of PVP to the silver facets can be explained by

Wulff's theorem, which states that atoms will reside on atomic planes to reduce interfacial free energy (γ). Equations 6, 7, and 8 evaluate the plane interfacial free energy for the {100}, {110}, and {111} planes, respectively, for a face-centred cubic crystal with atomic lattice spacing, a, and bond strength, ε.

$$\gamma_{100} = 4\left(\frac{\varepsilon}{a^2}\right),\ \gamma_{110} = 4.24\left(\frac{\varepsilon}{a^2}\right),\ \gamma_{111} = 3.36\left(\frac{\varepsilon}{a^2}\right) \qquad \textbf{(6, 7, 8)}$$

The affixation of PVP to high interfacial energy {100} planes reduces the overall energy of the system and elongates NWs by attachment of Ag atoms to the {111} planes.[32]

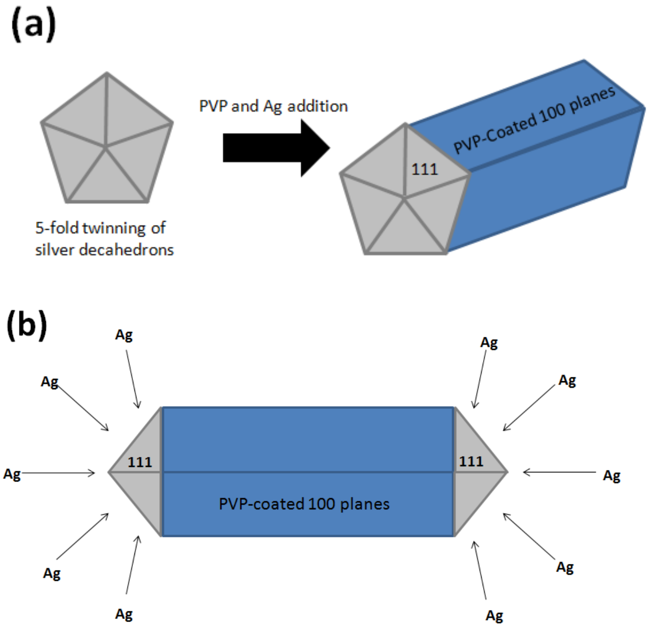

Figure 2.3: (a) Growth of Ag NWs from 5-fold twinned Ag tetrahedrons after addition of PVP and Ag. (b) Binding of Ag atoms to {111} faces after reduction of $AgNO_3$ by EG. Binding cannot occur on {100} planes due to PVP coating.

NW synthesis can be tuned significantly by control agents, which determine the diameter of the NW by forming a silver salt colloid seed for NW growth. Control agents also determine the growth rate of the NWs according to oxidation and reduction rates of the silver salt.[35] The control agent $CuCl_2$ is used for NW synthesis in this thesis due to the small diameter (less than 100nm) of resulting NWs and slow injection of Ag atoms from AgCl crystals.[36] Both the small diameter and slow injection are achieved because silver cations can hold both Ag(I) and Ag(II) valence states. Therefore, very small AgCl crystals can oxidize to form Ag^+ ions, which dissociate from the AgCl crystal and can attach to the {111} planes of growing NWs.[35]

Immediately after $AgNO_3$ is injected into the EG-PVP-control agent solution, the solution undergoes a series of colour changes.[35] Typically the solution changes from clear to yellow, then red-orange, then green, then to a dark grey that lightens significantly within the last hour of synthesis.[36,37,36] This phenomenon can be explained by interactions of electromagnetic waves with the growing nanocrystals, known as the plasmonic effect.[38]

When a metal nanostructure with dimensions less than the wavelength of light is placed under irradiation, photons of a given frequency will disturb unbound electrons from their respective equilibrium positions in the conduction band and move them to the surface of the metal.[34] The charge separation of the electrons from their equilibrium positions will provide the charge restorative force, only to be displaced once again by incoming electromagnetic waves, continuing the oscillation of the electrons within the nanostructure. The required restoring force will vary according to nanostructure geometry. As nanostructures increase in size, conduction electrons no longer move together in phase, thus reducing the depolarization field. Therefore, large nanostructures shift away from high-energy, ultra-violet and blue light absorption in favour of lower energy, longer wavelength light absorption, as observed with the growth of small nanocrystals to longer nanowires.[32]

Nanowire junctions are several orders of magnitude more resistive than typical NWs, thus the area and number of junctions should be minimized to achieve high conductivity NW films.[14] Longer, thinner NWs reduce junction area and produce high conductivity films for relatively low NW densities, functioning to both reduce the number of resistive junctions and increase film transparency. Because of this, NWs for TC fabrication should be as long and thin as possible.[33]

Once satisfactory NW synthesis is complete, NW deposition must be optimised in order to generate a NW network with optimal electrical and optical properties.

2.1.4.3 Nanowire Deposition

As mentioned in 2.4.1, a well-interconnected network of NWs is necessary to produce a low R_{sheet} film. Deposition of randomly oriented NW films has been achieved using spray coating, dip coating, mayer rod deposition and stamp transfer methods.[39,40,14] A vacuum filter stamping process was used to deposit NWs in this thesis due to the advantageous removal of small-aspect ratio nanowires and nanoparticles.[33]

Density of deposited NWs also impacts device performance. Nanowire density is a trade-off of high transmissivity at low NW densities for low R_{sheet} films at high NW densities.[30] Density-dependent TC performance is explored in greater detail in Chapter 5.

Once deposited, these NW films can be applied to a wide variety of optoelectronic devices.

2.1.4.4 Silver Nanowire Transparent Conductor Devices

Silver NW TCs have been proven to be effective in devices ranging from light-emitting diode displays and touch screens to PV cells.[41-43] Furthermore, Ag NWs can be deposited on a variety of substrates such as glass, plastic, and fabrics, with minimal performance degradation, allowing previously impossible materials to perform as conductive substrates.[44] This section reviews the current state of Ag NW TC devices and the opportunities for Ag NW TC improvement in device fabrication.

2.1.4.4.1 Standard Nanowire Electrodes and Touch Screens

The high Young's modulus of Ag NWs allows for high film flexibility and elasticity, allowing for 460% film strain before catastrophic failure of a NW conducting film. This phenomenon has been proven such that an array of LEDs connected by an Ag NW TC is still operational at strains above 400%.[32]

These attractive physical properties have been utilized by multiple groups to successfully fabricate a flexible touch screen using an Ag NW TC.[38,44] Touch screens fabricated by stamp printing of NWs maintain conductivity after 20,000 bending cycles as well as up to 10% strain.[38] This particular application of Ag NW TCs has been suggested to benefit wearable interactive electronics.[38] However, the highly desirable characteristics of Ag NW TCs can also be applied to light emitting diodes.

2.1.4.4.2 Light Emitting Diodes

Organic light emitting diodes (OLEDs) using an Ag NW TC base have been realized by multiple groups.[43,45] This is an important breakthrough, as OLEDs have stringent optical, electrical, and low surface roughness requirements for the TCs used in OLED fabrication.[45] In order to combat high roughness values attributed to Ag NW overlap and non-planar Ag NW orientation, Ag NWs were deposited on a polymer substrate which reduced film roughness to less than 5nm while maintaining R_{sheet} values of 11 Ω/sq and 87% transparency.[40]

2.1.4.4.3 Current Silver Nanowire Solar Cells

Thus far, the only reported solar cells using an Ag NW TC have used an organic photoactive layer.[46,47,42] The highest Ag NW solar cell, fabricated using a photosensitive P3HT:PCBM layer, achieved a power conversion efficiency (PCE) of 3.8% and 3.2% on a glass and flexible substrate, respectively.[42]

The random network of Ag NWs and sloping circumference of NWs promote a large amount of photonic scattering upon illumination. Scattering angles in NW solar cells >10° have been found to increase the optical path length within the cell, thus providing greater opportunity for exciton-generation and increasing photocurrent values over 19%.[16]

Although these Ag NW-organic solar cells are all-solution processed and offer the potential for inexpensive PV modules, diffusion of oxygen and water into the organic layer rapidly degrades the PV devices.[48] These issues provide incentive to utilize other solution-based photosensitive materials, to fabricate a low-temperature, solution processed, inorganic Ag NW TC solar cell. Solar cell operation and characterization must be understood in order to fabricate such devices.

2.2 Fundamental Physics of Solar Cells

Sunlight consists of packets of electromagnetic energy called photons, which are of varying energy density according to photon wavelength.[49] Despite the fact that solar energy is available at wavelengths up to 2500nm, the visible region of the solar spectrum, consisting of wavelengths of 300-800nm, offers the greatest solar energy density ranging from 1.77 eV to 3.10 eV.[50]

The photoelectric effect, the production of excited electrons caused by the absorption of light by a metal sample, was first observed by Edmund Bequerel in 1839. This phenomenon, caused by material-dependent energy levels, is utilized by solar cells in order to produce a usable current.[49]

2.2.1 ENERGY BAND STRUCTURES

Each atom of a solid material possesses a given number of electrons with intrinsic energy values dictated by electron orbital and rotation. When a series of atoms are compressed together in a bulk solid, the distinct electron energies distort due to electron wave function interactions with adjacent atoms. The result of this is a number of continuous "bands" of energy states at which an electron can rest, each associated with a particular electron orbital and spin.[51] Each of these energy bands is separated by a number of energy levels which cannot be produced by any combination of available wave functions and thus cannot be occupied by an electron. The unoccupied region between the highest fully-occupied energy band (valence band) and the lowest empty or semi-filled energy band (conduction band) is known as the "energy gap", E_g, of the material.[50]

As Figure 2.4 indicates, the nature of these energy bands and size of E_g defines an electronic material as an insulator, semiconductor, or conductor.[51] Of greatest interest to solar cells are semiconductors, such as silicon, which have the unique property that E_g is relatively small (~1.1 eV). When a photon of greater value to the E_g strikes a semiconductor, an exciton is generated; wherein an electron is excited from the valence band to the conduction band, leaving an unoccupied state, or "hole", in the valence band. After separation across the band gap, the electron-hole pairs can be collected as usable current. Because the E_g of a semiconductor is on the same scale as the highest energy density of the visible light region, semiconductors such as GaAs and Si are desirable photovoltaic materials for PV modules.[51]

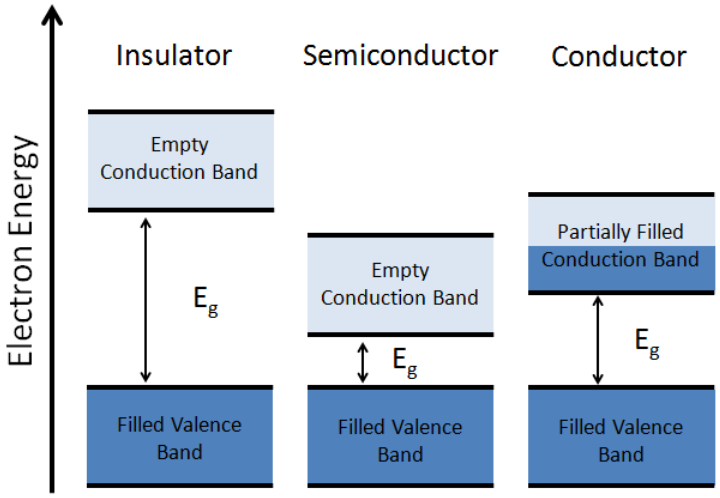

Figure 2.4: Three material energy-band structures. A conductor has a partially filled conduction band, whereas both an insulator and a semiconductor contain no electrons within the conduction band. The difference between an insulator and a semiconductor lies in the size of the E_g, as the large E_g of an insulator prevents an excited electron from occupying the conduction band, whereas the relatively small E_g of a semiconductor enables sufficiently excited electrons from the valence band to occupy energy states in the conduction band.

Determining the desired E_g of a solar cell is a trade-off between competing characteristics: producing a high current density (J), which requires a large flux of photons of $E>E_g$, and producing a current with a significantly large voltage (V), requiring a device with a large E_g. Therefore, as the E_g increases, the produced V increases, but J decreases due to the reduced number of photons available of $E>E_g$ to excite electrons to the conduction band. Optimising these competing cell conditions, it has been determined that an E_g of ~1.4 eV will result in the highest performing cells.[49]

2.2.2 PHYSICS OF P-N JUNCTIONS

Standard photovoltaics are in principle a p-n junction, where an “n-type” semiconductor (containing a higher concentration of electrons) is placed in proximity with a “p-type” semiconductor (containing a higher concentration of holes). Recombination of electrons and holes from the n and p-type semiconductors, respectively, results in an intrinsic region at the p-n junction called the depletion region. The diffusion of electrons and holes away from the n and p-region, respectively, gives rise to an internal electric field (E_o), which acts to counter charge diffusion. The equilibrium of diffusion forces and E_o dictates the depletion width, the physical distance where the semiconductor is undoped, shown in Figure 2.5.[51]

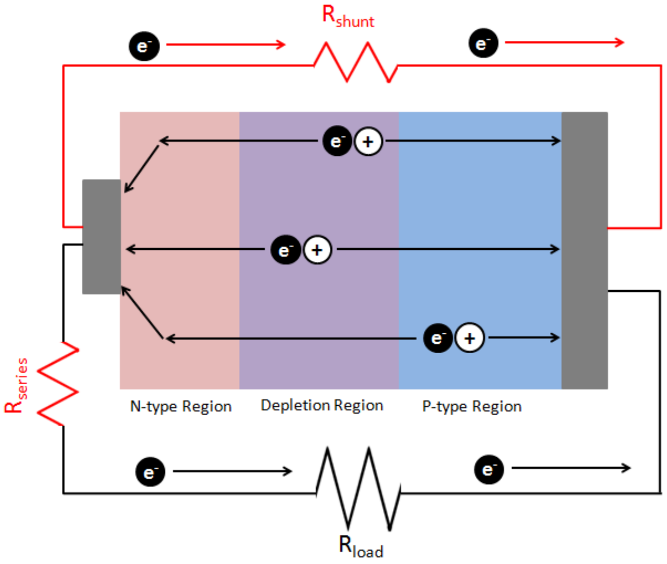

Figure 2.5: Standard p-n solar cell, where excitons are generated and charges separate within the depletion region (purple) or within the minority carrier diffusion length of the depletion region, so E_o can sweep minority charges across the depletion region for collection by the opposite contact. Parasitic resistances are denoted in red and intended pathways for charges are outlined in black.

The depletion width is important because excitons generated within the depletion region are forced by E_o to drift to the junction interface for separation and collection.

Excitons generated within an excitonic diffusion length of the depletion region can also diffuse to the boundary of the depletion region for charge collection. Excitons generated beyond the carrier diffusion length from the depletion region will recombine.[51] After separation at the p-n junction, these charges are removed from the device as usable current.[51] The extracted photocurrent generated by a solar cell across a spectrum of applied voltages can be graphed as what is known as a J-V curve, as seen in Figure 2.6. Particular values extracted from the J-V curve determine the quality of the solar cell.

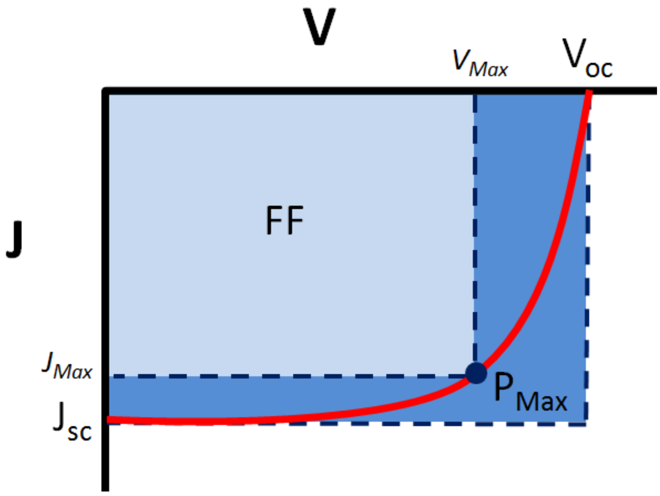

Figure 2.6: Standard J-V curve for a PV device, graphing the produced photocurrent density for applied bias values between 0V (voltage resulting in J_{sc}) and V_{oc} (greatest V-value, resulting in 0 photocurrent density). The fill factor (FF) is the light blue fraction of the dark blue rectangle. The light blue area is dictated by J_{Max} and V_{Max}, the current density and voltage values which result in P_{Max}, the maximum power obtainable from the device.

2.2.3 QUALITY MEASUREMENT OF PHOTOVOLTAICS

Two values which can be extracted from a solar cell J-V curve, the open-circuit voltage (V_{oc}) and the short-circuit current density (J_{sc}) are vital to quality measurement of photovoltaics. The V_{oc} is the maximum voltage difference between the two doped semiconductive materials which develops if the terminals connecting the cell are disconnected, equivalent to an infinite load resistance. The J_{sc} is the maximum current density which can develop in the case of short-circuiting, or zero resistivity.[49] These values are benchmarks which can be used to pinpoint the source of efficiency loss within a cell.

When a solar cell is illuminated and connected to a resistive load, the voltage and photocurrent density values will be between 0 and V_{oc} and J_{sc}, respectively. Equation 9 demonstrates that the power density delivered by the cell is given by the product of the photocurrent density, J, at its respective voltage.

$$P = JV \qquad \textbf{(9)}$$

The maximum power density obtainable (P_{Max}) is the highest product for some voltage V_{Max} and corresponding photocurrent density, J_{Max}. Equation 10 calculates another important figure of merit for solar cell performance known as the cell fill factor (FF), which compares P_{Max} to the power density of the product of V_{oc} and J_{sc}.

$$FF = \frac{J_{sc}V_{oc}}{J_{Max}V_{Max}} \qquad \textbf{(10)}$$

The FF is especially important as it indicates the “squareness” of the J-V curve, which can identify either the J_{sc} or the V_{oc} as the source of efficiency-loss.[49]

The overall conversion efficiency of the solar cell, η, can be calculated using Equation 11, which compares the maximum power density produced by the PV device to the solar power density, P_S.

$$\eta = \frac{J_{Max}V_{Max}}{P_S} \qquad \textbf{(11)}$$

An ideal J_{sc} is the direct conversion of every incident photon into a collectable exciton. As noted in 2.2.1, if the energy of the photon (E_{photon}) does not surpass E_g, a photocurrent-contributing exciton cannot be produced. Not surprisingly, as E_g of the semiconductive material decreases, J_{sc} increases, as lower energy photons are capable of producing excitons, with the caveat of a lower V_{oc}. Some physical conditions reduce J_{sc}, such as reduced photon absorption due to reflectivity or transmission and light-blocking metal-contacts. From an electrical view, J_{sc} can also be reduced by recombination of electron-hole pairs which typically arises at defects or when exciton-generation takes place at distances greater than the minority carrier diffusion length from the p-n junction. Therefore, reducing the size and number of defects, broadening the depletion region, and increasing minority carrier lifetime will result in large J_{sc} values.[52]

V_{oc} increases with the size of E_g, resistivity (of the load as well as at the contacts), and light intensity. V_{oc} is also reduced by phonon generation caused by recombination in trapping states, resulting in increased cell temperature.[52] Sources of cell degradation, known as parasitic resistances, must be identified for optimal cell design and processing.

2.2.4 PARASITIC RESISTANCES

Parasitic resistances in non-ideal solar cells are common sources of reduced J_{sc} and V_{oc} values, leading to overall reduced cell conversion efficiency. The electrical circuit diagram of cells with included parasitic resistances, series resistance (R_{series}) and shunt resistance (R_{shunt}), are shown in Figure 2.5. Optimised solar cells will achieve a low R_{series} and a high R_{shunt}. A high R_{series} typically arises due to poor contacts or poorly conductive TCs, which reduces J_{sc} due to undesired current dissipation. A low R_{shunt} is caused by leakage paths (current pathways between opposing contacts or around the edge of the cell) which divert the photocurrent in parallel to the external load, thus decreasing the V_{oc} of the cell.[51]

The source of degradation of a cell can be pinpointed to either R_{shunt} or R_{series} by inputting data from a cell J-V curve into Equation 12 and Equation 13, respectively.[53,54]

$$\frac{dV}{dI}|_{I=I_{sc}} = R_{shunt} + R_{series} \approx R_{shunt} \qquad \textbf{(12)}$$

$$\frac{dV}{dI}|_{V=V_{oc}} \approx R_{series} \qquad \textbf{(13)}$$

It should be noted that current (I), rather than current density (J) is used for these equations, as the cell size does not dictate the magnitude of R_{shunt} nor R_{series} values.

Reverse saturation current density (J_o), which indicates the magnitude of diffuse minority carriers in reverse bias under dark conditions, is another parameter which can be used to evaluate cell performance. J_o will be relatively small (~10^{-6} A/cm^2), as the energy barrier at the p-n junction is increased. However, in the case of a short-circuiting cell, the value of J_o will increase by several orders of magnitude due to the significant decrease in barrier height. J_o can be fit to dark J-V curve data using Equation 14, where q, k_B, and T are the electronic charge value, Boltzmann constant, and temperature (K), respectively. The diode ideality factor (*n*) varies by PV material and structure. For an ideal diode, the ideality factor is equal to 1. However, defects, resulting in recombination sites, often cause the diode ideality factor to increase slightly. Generally speaking, the closer *n* is to 1, the higher quality the diode.

$$J = J_o(\exp\left(\frac{qV}{nk_BT}\right) - 1) \quad \textbf{(14)}$$

A low R_{series} ($<20\Omega$-cm^2), a high R_{shunt} ($\geq 10k\Omega$-cm^2), and a low J_o is needed to achieve both high J_{sc} and V_{oc} values for high efficiency solar cells.[49] Understanding of basic solar cell operation from this section will now be applied to quantum dot photovoltaic devices.

2.3 Quantum Dot Photovoltaics

Quantum dots (QDs) are semiconductor nanocrystals on the order of 1-100nm and are typically composed of 10^2-10^7 atoms.[55]

2.3.1 OVERVIEW OF QUANTUM DOTS

As discussed in 2.2.1, when multiple atoms of a semiconductor are brought into close proximity, the individual atomic electron energy bands overlap to generate a continuous band of energy states separated by some unobtainable energy levels which comprise E_g. It should be noted that Figure 2.4 is representative solely for *bulk* materials. Figure 2.7 is a diagram of the merging of bands of a semiconductor from a single atom to a QD of at most ~10^4 atoms to a bulk material containing >>10^4 atoms. Unlike bulk semiconductors, QD electrons are not limited to distinct bands but can also occupy multiple energy states separate from the primary continuum of energy states.[56]

The scientific importance of QDs is derived from the definition of the de Broglie wavelength of a particle:

$$\lambda = \frac{h}{p} \quad \textbf{(15)}$$

as well as the energy value associated with that particle,

$$E = h\frac{v}{\lambda} = pv \qquad \textbf{(16)}$$

where h = Planck’s constant, p = particle momentum, and v =velocity of the particle.

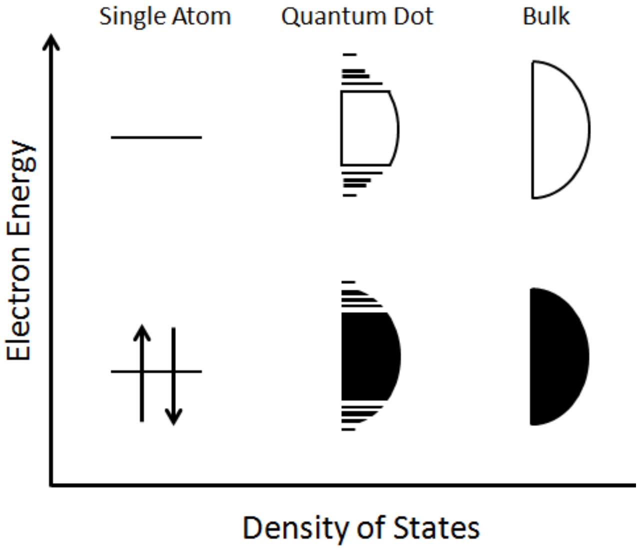

Figure 2.7: Energy states for semiconductor material as a single atom, QD and in bulk. The atom offers two singular energy states, one fully occupied and one unoccupied. Some overlap of energy states arise with increased number of atoms in a QD, however some individual energy states still exist that are separate from the largest region of energy states. In bulk, two distinctly separate energy bands exist, separated by a given E_g.

The Heisenberg uncertainty principle for position and momentum states that it is impossible to precisely determine both the physical location and the momentum of a particle at a single point in time because as one characteristic is more accurately measured, there is greater uncertainty in regards to the measurement of the other characteristic.[51] This applies to QD theory because the movement of electrons within a QD is restricted compared to the bulk material so there is reduced uncertainty of particle position in a QD than in bulk and consequently greater uncertainty in regards to particle momentum. The greater variability of p values results in greater variability of generated energy values, which gives rise to energy states in QDs which are inaccessible in the bulk material.[56] The E_g can be altered according to the diameter of the QD because as the diameter decreases and the position uncertainty decreases, a greater number of energy states are available due to greater momentum variability. Smaller QD diameters thus lead to an increase in E_g as the spectrum of densely occupied energy states decreases in favour of a greater number of sparsely occupied energy states.[55]

2.3.2 OPERATION OF QUANTUM DOT SOLAR CELLS

Like standard solar cells, when a photon of $E_{photon} > E_g$ illuminates a semiconductive QD, an exciton is generated and the charges can be collected with the application of an electric field to the device.[55] However, QD solar cells can be produced at lower cost because of the relatively low temperatures needed for QD growth ($<200^{0}$C) and the capability for high-throughput QD solar cell fabrication via a rapid roll-to-roll process or ink-jet printing using QD ink.[57,58]

Although QDs can be fabricated from a variety of semiconductive materials, [59-62] lead sulphide (PbS) QDs were selected for device fabrication for this thesis due to their strong quantum confinement. This strong quantum confinement produces high V_{oc} values and improved charge transfer between neighbouring QDs for high photocurrent generation.[57,63,64] Once QDs have been synthesized, a ligand exchange is required for high efficiency solar cell fabrication.

2.3.3 LIGANDS

Intrinsic high surface area to volume ratios make QDs particularly sensitive to oxidation and other forms of chemical corrosion. Long chain ligands are thus required to passivate these sensitive surfaces from chemical degradation during synthesis.[65] However, ligands used for QD synthesis (typically oleic acid) are electrically insulating, necessitating a replacement of synthesis ligands for shorter, less insulating ligands for quality device fabrication in order to extract a photocurrent before charge recombination can occur.[66]

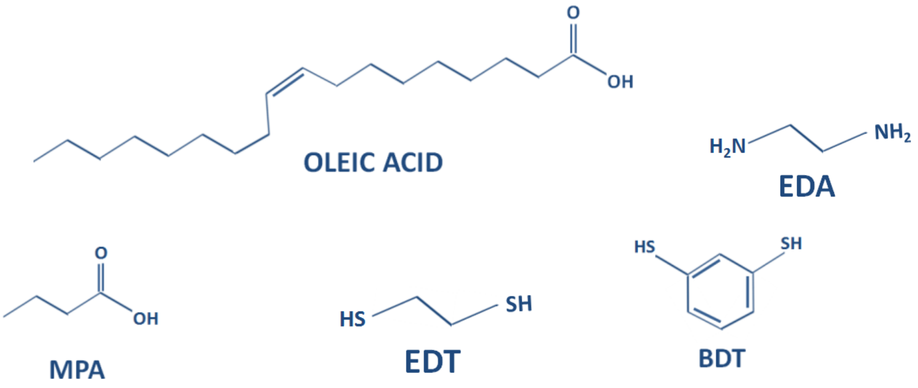

Figure 2.8: Common organic ligands used in QD synthesis and QD solar cell fabrication

The ligands chosen to replace oleic acid are selected based upon length, which determines QD spacing, functionality (establishing cross-linking versus singular QD-binding), anchor group, and chemical properties which may enhance or diminish charge transfer between QDs. Figure 2.8 features some of the most common ligands used for QD synthesis and solar cell fabrication. Thiols, sulfhydryl carbon compounds, such as 1,2-ethanedithiol (EDT), 1,4 benzenedithiol (BDT), and mercaptoproprionic acid (MPA), have attracted much attention for their short interdot spacing, enhanced QD cross-linking, and capability to remove insulative oxygen shells on PbS QDs.[67,68] Shorter ligands are typically preferred in order to provide shorter charge-carrier lengths between QDs, although some longer ligands have produced higher efficiency QD devices due to greater trap passivation.[69] Longer ligands also have the added benefit of reduced film cracking, which can cause current loss.[65]

EDT was the fabrication ligand of choice for this thesis, as many research teams have used it to produce highly conductive PbS films upon oleic acid removal.[64,70,71] Cell structure, in addition to ligand exchange, also plays an important role in the determination of device performance.

2.3.4 QUANTUM DOT SOLAR CELL DESIGN

Three QD solar cell structures currently dominate the field: 1) a Schottky cell consisting of a photosensitive QD layer between two metal contacts, 2) a QD-depleted-heterojunction solar cell (QD-DHSC), employing a large E_g layer between the QD layer and the exciton-extracting electrode [72], and 3) an organic-inorganic device in which the QDs are embedded in a conductive polymer, the last of which is outside the scope of this thesis.[73]

Figure 2.9a illustrates the structure of the Schottky cell and the band diagram for this device, whereas Figure 2.9b illustrates the modified Schottky cell structure and band diagram with a large E_g material, resulting in a QD-DHSC. The large E_g layer in a QD-DHSC acts as a barrier to the holes which otherwise can migrate into the electron-extracting contact, thereby reducing the J_{sc} of the device.[72]

A variety of wide E_g materials have been used in QD-DHSCs, including SnO_2, TiO_2, and ZnO.[74,75,76] Charge extraction can increase substantially using a bulk heterojunction device structure due to the large contact area between the photosensitive material and the charge-extracting oxide layer.[77] For this reason, a ZnO heterojunction layer was utilized in cell fabrication for this thesis. Consideration of charge separation in these devices is necessary to optimise QD and ZnO layer thickness.

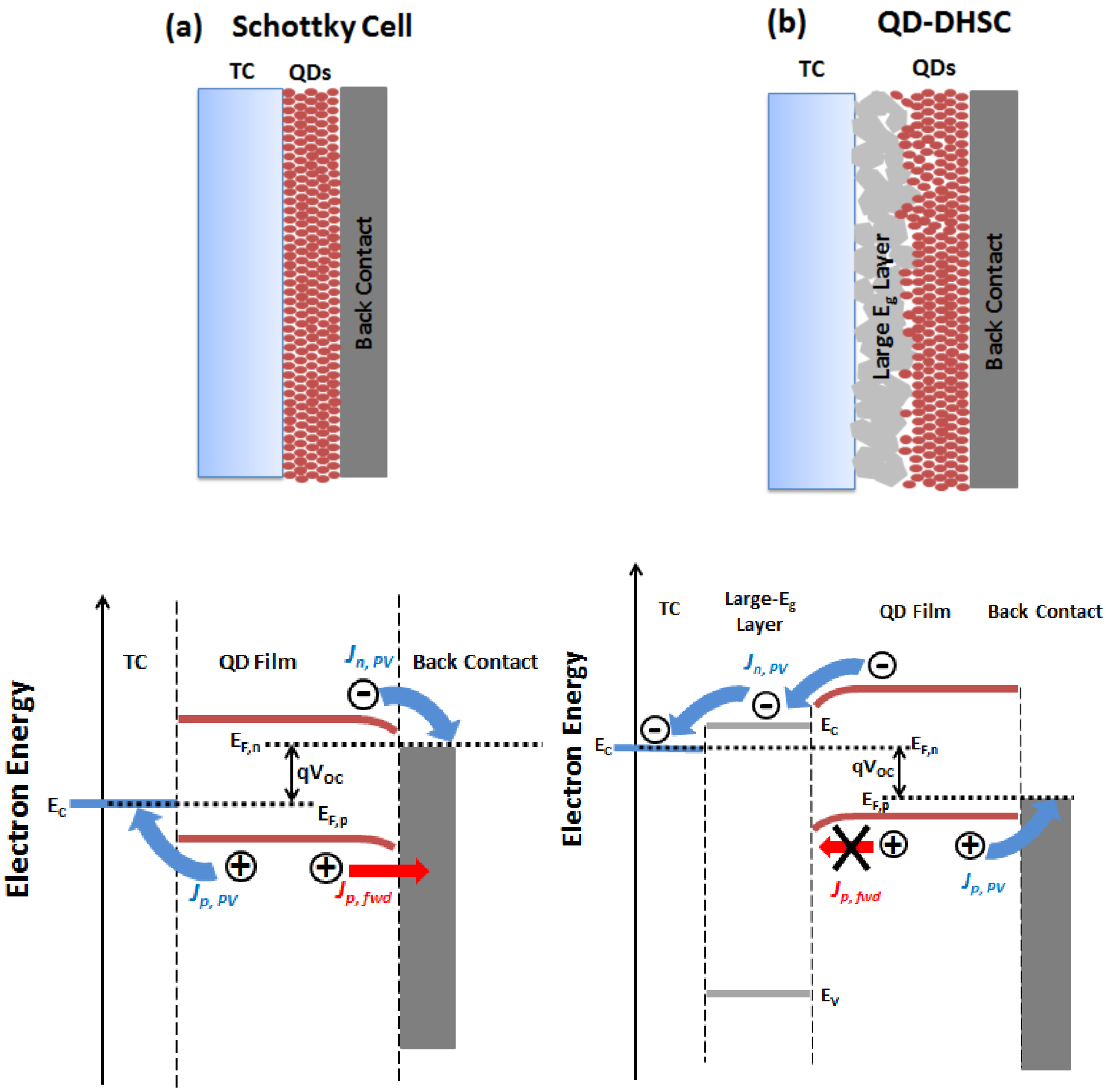

Figure 2.9: (a) Schottky cell and (b) QD-depleted heterojunction solar cell (QD-DHSC) device structure and energy diagram. The wide E_g material in the QD-DHSC improves device efficiency by blocking leakage of $J_{p,fwd}$ which reduces overall J_{pv} in the Schottky cell by electron-hole pair recombination.

2.3.5 QUANTUM DOT HETEROJUNCTION SOLAR CELLS

The mechanism of charge separation in heterojunction QD solar cells has been a subject of much debate. There have been cited instances of the ZnO-PbS QD junction operating as an excitonic junction[78,64] as well as a depleted p-n junction.[72,79] Diagrams of charge generation and collection for both of these devices are depicted in Figure 2.10.

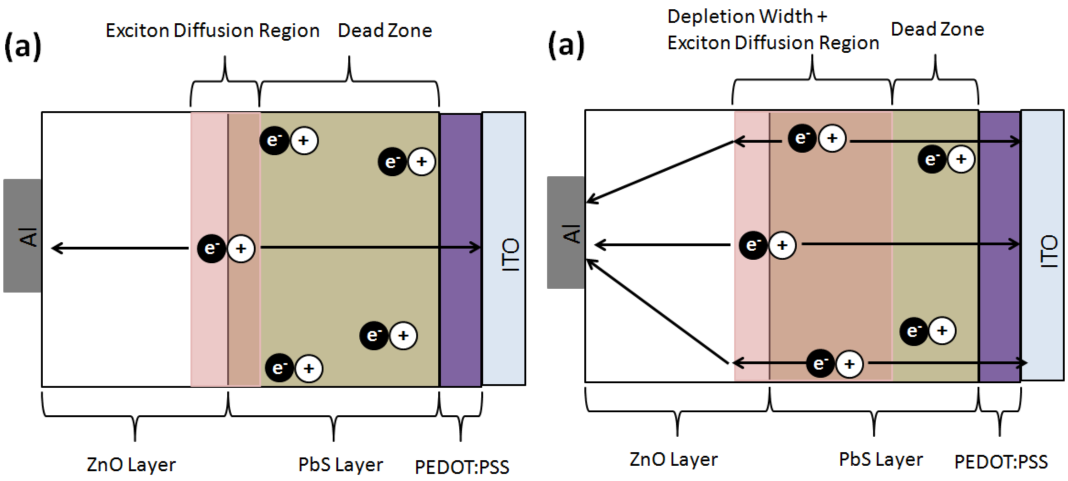

Figure 2.10: (a) Charges in an excitonic QD solar cell can only be collected within an exciton diffusion length of the ZnO-PbS QD interface (pink), where they are separated for usable current. All excitons generated in the dead zone (beige) will recombine before charge separation can occur. (b) Charges in a QD solar cell operating as a p-n junction can be collected within the depletion region of the junction and within an exciton diffusion length of the depletion width.

As described in 2.2.2, excitons developed within a minority charge carrier diffusion length of the depletion region will be swept away by the built-in electric field of the depletion region and collected for usable current.[51] Excitonic cells diverge from traditional P-N junction cells because electron-hole pairs are tightly bound, thus can travel only very short distances before recombining. Therefore, as long as excitons are generated within an excitonic diffusion length of the junction interface and the band offset is greater than the excitonic binding energy, these charges will be separated. This limitation results in a large "dead zone" in excitonic cells, wherein generated excitons recombine before charge carrier separation.[80] A p-n junction solar cell is thus desirable, due to greater opportunity for charge separation and collection.

Significant evidence supports the theory that quality QD solar cells operate as a p-n cell.[81,71] Nonetheless, Johnston et al. observed poor charge collection for excitons generated within the diffusion region of the depletion width, primarily due to poor charge carrier mobility within the QD layer.[81] Performance enhancement is achievable for both p-n and excitonic junctions by increasing the interface area of the PbS QD-ZnO junction to provide more sites for charge carrier separation.[79]

Heterojunction structures have further been improved using a variety of nanoporous structures, generally classified as bulk heterojunction (BHJ) solar cells.[82,83] High QD-ZnO interfacial area allows for greater exciton dissociation and collection to achieve higher PCE values.[84]

2.3.6 CURRENT STATE OF QUANTUM DOT SOLAR CELLS

As of 2013, Sargent et al. have achieved the record QD solar cell efficiency of 8.5% using a PbS QD-TiO_2 depleted-heterojunction cell. This device was fabricated by depositing a 10nm TiO_2 film on fluorine doped tin oxide (FTO) by atomic layer deposition (ALD). Subsequently, ~380nm of PbS QDs were deposited using an MPA ligand exchange to replace the oleic acid synthesis ligands. Finally, a multilayer MoO_3/Au/Ag top contact was deposited by multiple evaporation steps.[85]

While the high PCE achieved by this group is admirable, the slow-throughput, high-vacuum ALD required to achieve this device structure is outside the scope of this thesis. Therefore, an alternative PbS QD cell structure was used in this thesis, as described in greater detail in the next chapter.

2.3.7 CONCLUSIONS

Background research indicates that substitution of ITO for silver nanowire transparent conductors in photovoltaics is possible, but has only yet been realised for organic solar cells. Because high efficiency devices have been achieved using PbS QDs, an EDT ligand exchange, and a ZnO heterojunction layer on ITO,[64] devices in this thesis were fabricated using these techniques. The details of device fabrication will be covered in the next chapter.

CHAPTER 3 - EXPERIMENTAL METHODS

3.1 Nanocrystal Synthesis

3.1.1 SILVER NANOWIRE SYNTHESIS

The Ag NWs used for device fabrication were synthesized using the polyol process described in 2.1.4.2. 5mL EG was heated at approximately 152^{0}C for 1 hour in an ambient environment while stirring.[86] In a separate vial, a 4mM $CuCl_2{\cdot}2H_2O$-EG solution was produced by combining 3.4mg of $CuCl_2{\cdot}2H_2O$ with 5mL of EG. Separately, a 0.147M poly(vinyl pyrrolidone) (PVP) solution was prepared by adding 0.024g of 50,000 MW PVP to 1.5mL EG and a 0.094M $AgNO_3$ solution was prepared by adding 0.024g of $AgNO_3$ to 1.5mL EG.

After 1 hour of heating, 40µL of the $CuCl_2{\cdot}2H_2O$ solution was added to the 5mL of heated EG. After an additional 15 minutes of stirring at 152^{0}C, 1.5mL of PVP solution, followed by 1.5mL of $AgNO_3$ solution was added.[35,36] This solution remained stirring at 152^{0}C for two hours before removal from heat. As mentioned in Chapter 2, the initiation of nanocrystal growth was confirmed when the solution changed from a clear solution to a pale yellow, dark yellow, and then orange within the first 40 minutes of synthesis. By the end of the 2 hour NW synthesis, the solution was a light grey colour.

The Ag NW solution was centrifuged in acetone (10 minutes, 3000rpm) and subsequently centrifuged 3 more times in methanol (10 minutes, 3000rpm).[36] After the last centrifugation, the solution was decanted and the Ag NWs were finally redispersed in 2.6mL of methanol for a 1.25wt% NW solution.

3.1.2 PBS QUANTUM DOT SYNTHESIS

The PbS QDs used in this study were synthesized by a fellow DPhil student, Chi (Darren) Neo, using previously published methods.[57] To synthesize PbS QDs, 0.46g PbO, 10g 1-octadecene (ODE), and 2g oleic acid (OA) were stirred vigorously in a three-neck flask at 90^0C under vacuum for 3 hours until the PbO was dissolved and the solution appeared clear. In a N_2 drybox, 210μL of hexamethyldisilathiane $(TMS)_2S$ was combined in a separate vial with 5g ODE before subsequent loading into a syringe. After three hours of heating, the PbO solution was raised to 120^0C and switched from vacuum to N_2 flow. Nanoparticle nucleation was then induced by rapid injection of the $(TMS)_2S$ solution into the PbO mixture, indicated by the solution colour change from clear to dark. The heating plate was switched off but the flask was not removed to allow nanocrystal growth to continue for 20-30 minutes, producing QDs with an average $E_g \approx 1.3$-1.4 eV.

After synthesis, the nanocrystals must be removed from the rest of the solution and any undesirable side-products of QD synthesis. In order to do this, the cooled solution was centrifuged with acetone and the supernatant was decanted. The remaining PbS QDs were redispersed in 5mL hexane and centrifuged in methanol for further cleaning. This supernatant-decanting, hexane-redispersal, and methanol centrifugation was performed once more before the QDs were finally dispersed in toluene at a concentration of 50mg/mL to be used for spin coating deposition of the QDs.

3.1.3 ZNO SYNTHESIS

ZnO was prepared using a previously published solution process by Pacholski et al. 2.2g zinc acetate dihydrate was dissolved in 100mL methanol and stirred vigorously on a hot plate at 60^0C. Once the zinc acetate solution temperature stabilized, 1.1g KOH, dissolved in 50mL methanol was added dropwise under continuous stirring and heating (60^0C). The ZnO nanocrystals grew at 60^0C under continuous stirring for 2.5 hours before removal from heat. The solution was centrifuged in methanol 3 times via centrifugation at 3000rpm for particle collection and cleaning. The ZnO precipitates were collected and redispersed in chloroform at a concentration of 50mg/mL.[87]

3.2 Transparent Conductor Fabrication

As previously mentioned in 2.1.2, the two most critical characteristics of typical transparent conductors (TCs) are transparency and electrical conductivity. Vacuum filter deposition and a post-deposition heat-treatment were used together to maximize these two qualities.

Vacuum filter deposition, demonstrated in Figure 3.1, was used to deposit Ag NWs onto 1.2cm x 1.4 cm glass substrates to fabricate the Ag NW transparent conductor later used in PV devices. Vacuum filter deposition is desirable because it removes silver nanoparticles and shorter NWs, which do not contribute significantly to electrical conductivity, in the process of depositing NWs on the glass substrate.

For each TC fabricated, the vacuum filter pump was switched on and a filter paper (Omnipore ™ hydrophilic PTFE 25mm, 10μm diameter pores) was placed on the glass filter surface. A low concentration Ag NW-methanol solution (0.016wt%) was deposited dropwise on the filter paper in a line approximately 5mm wide and 20 mm long.

After the desired volume of Ag NW solution was deposited, the glass substrate was placed on top of the filter paper until all of the liquid was removed. The pump was then switched off and both the glass substrate and the filter paper were inverted and placed back on the glass vacuum filter, with the pump switched on. Methanol was deposited dropwise on the filter paper, improving Ag NW adherence to the glass substrate due to high capillary pressure provided by the fluid passing through the very small filter pores.

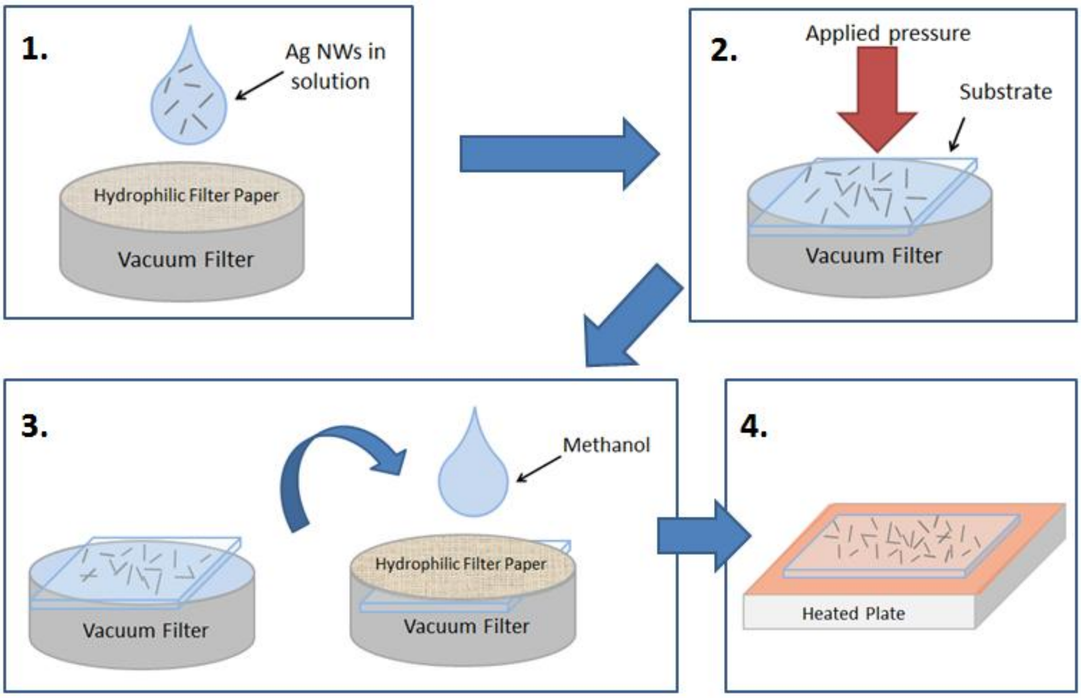

Figure 3.1: Ag NW deposition on glass substrate using vacuum filter deposition. 1. Ag NWs in solution were deposited on hydrophilic filter (pore size 10μm), removing all low-aspect ratio nanocrystals. 2. Glass was placed on top of NW-coated filter paper. 3. After 90sec, the pump was turned off and the filter paper and substrate were inverted on the glass filter surface. Methanol was deposited dropwise on the back side of the filter paper, increasing NW adhesion to the glass surface by capillary force. 4. Substrate was inverted and placed on hot plate to reduce junction resistivity of Ag network.

Once the methanol was completely removed, the NW-coated glass was placed on a hot plate at 200^{0}C for 2 hours (NW side facing up) to reduce resistivity at NW junctions by several orders of magnitude. After heat treatment, the Ag NW TC was shaped into a conductive strip, 1.4cm long and 2mm wide, using a combination of toothpicks and lint-free cotton buds. Two contact points of Ag conductive paint were finally deposited at either end of the Ag NW strip, as indicated in Figure 3.2a.

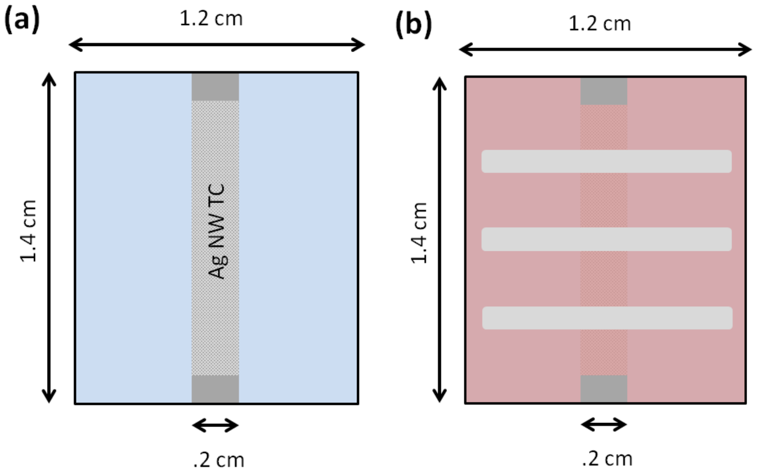

Figure 3.2: (a) Glass substrate with 2mm-wide deposited Ag NW TC. Dark grey rectangles at the two ends of the Ag NW TC indicate electrode connection points made of Ag conductive paint. (b) Complete device structure after PEDOT:PSS, PbS QD, ZnO deposition and Al contact evaporation. Each of the three light grey rectangles correspond to 1mm wide Al strips, such that each device produced contains three individual cells, each of area ~.02cm^2.

3.3 Device Fabrication

After Ag NW TC fabrication, three subsequent materials were deposited before evaporation of the aluminium contact shown in Figure 3.3.

A 30 second air (primarily N_2) plasma treatment was applied to the Ag NW TCs before spin coating of poly(3,4-ethylenedioxythiophene) oxidized with poly(4-styrenesulfonate) (PEDOT:PSS) for 1 min at 3000rpm. After spin coating, the substrates were heated at 150^0C for 20 minutes in order to remove residual H_2O from the PEDOT:PSS.

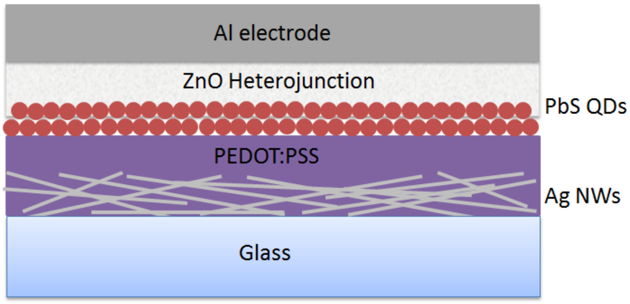

Figure 3.3: Cross-section view of Ag NW-PbS QD solar cell. Layer thicknesses not to scale.

Multiple layers of the QD-toulene solution prepared in 3.1.2 were deposited by spin coating. Large PbS agglomerations were removed from the QD solution by depositing the QDs through PTFE syringe filters (.45 µm pore size). For each layer of PbS deposited, a single drop of the QD solution was deposited while the substrate was spinning at 2000rpm. Immediately following PbS deposition while the substrate was still spinning, 2 drops of 1% volume EDT in methanol was deposited, followed by 5 drops of methanol, 5 drops of toluene and another 5 drops of methanol. This spin coating procedure was repeated for thicker photoactive films, with the standard device for this study consisting of 5 PbS layers. An exception to this was a study of the effects of photoactive layer thickness on device performance, discussed in 6.3.

After this point, 85µL of prepared ZnO solution was spun coat for 1 minute at 1000rpm. This ZnO deposition process was later altered, to be described in greater detail in 6.1.

Finally, a 100nm Al contact was evaporated on top of the ZnO layer, using a mask with three 1mm-wide slits, corresponding to the three contacts seen in Figure 3.2b.

CHAPTER 4 - CHARACTERISATION TECHNIQUES

High electrical conductivity and high transparency are the two most important characteristics for high-quality TCs. However, for thin-film devices such as QD solar cells, high roughness values can also play a crucial role in device performance, as highly rough films are prone to short-circuiting. Reflectivity of a TC can also reduce QD solar cell performance due to reduced photon penetration into the photosensitive layer. Five Ag NW densities were assessed for transparency, reflectivity, R_{sheet} and roughness quality using the techniques listed below.

4.1 DekTak Profilometer

A Veeco DekTak 6M Stylus Profilometer was used to assess the average thickness of each of the five Ag NW densities evaluated. This equipment operates using a diamond-tipped stylus which takes electromagnetic measurement as it scans over the desired sample surface. Over the course of a scan, the stylus moves up and down in the z-direction due to variations in the film surface. This vertical movement corresponds to an electrical signal of proportion to the stylus displacement, with a thickness measurement range of 50 Å to 100s of µm.[88]

This technique was used to assess the average thickness of a NW film according to volume of Ag NW solution deposited on the substrate, as well as the film thickness for deposited PbS layers.

4.2 Four Point Probe

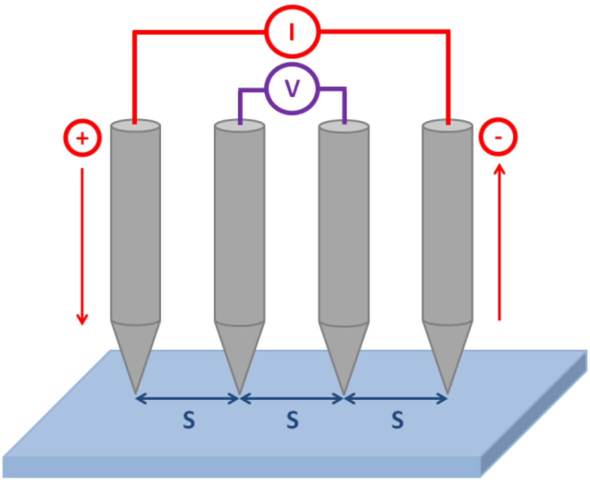

Figure 4.1: Diagram of four point probe, with four equidistant probes, the two outmost acting as the source and drain of current across the substrate and the inner two probes measuring the resulting electrical potential.

A four point probe measures R_{sheet} by applying 4 electrical contacts to a conductive film and passing a current between the two exterior contacts, shown in Figure 4.1. The resulting voltage, ΔV, is then measured between the two inner contacts. R_{sheet} can be calculated using Equation 17a, where s_1 and s_2 are the distances from the current source (outer probe) to the inner two probes.

$$\Delta V = \frac{I \times \mathrm{R_{sheet}}}{2\pi} \ln\left(\frac{s_1}{s_2}\right) \qquad \textbf{(17a)}$$

Because the two current-carrying probes are equidistant, $\ln\left(\frac{s}{s_2}\right)$ is simplified to ln(2). Furthermore, sufficiently thin films represent a dipole where $V = 2I \times R$, such that Equation 17a can be rearranged in order to solve for R_{sheet}.[89]

$$R_{sheet} = \frac{\pi}{\ln(2)} \frac{V}{I} \qquad \textbf{(17b)}$$

4.3 Integrating Sphere

Scattering effects of silver can greatly vary the optical path of incoming photons [16]. Because of this, standard methods of transmission and reflectance measurements which account for only specular light angles prove insufficient for Ag NW TC evaluation. An integrating sphere, which can differentiate the specular and diffuse reflection and transmission of a sample, was used for both TC transmission and reflectance measurement (Figure 4.2a and 2b, respectively).

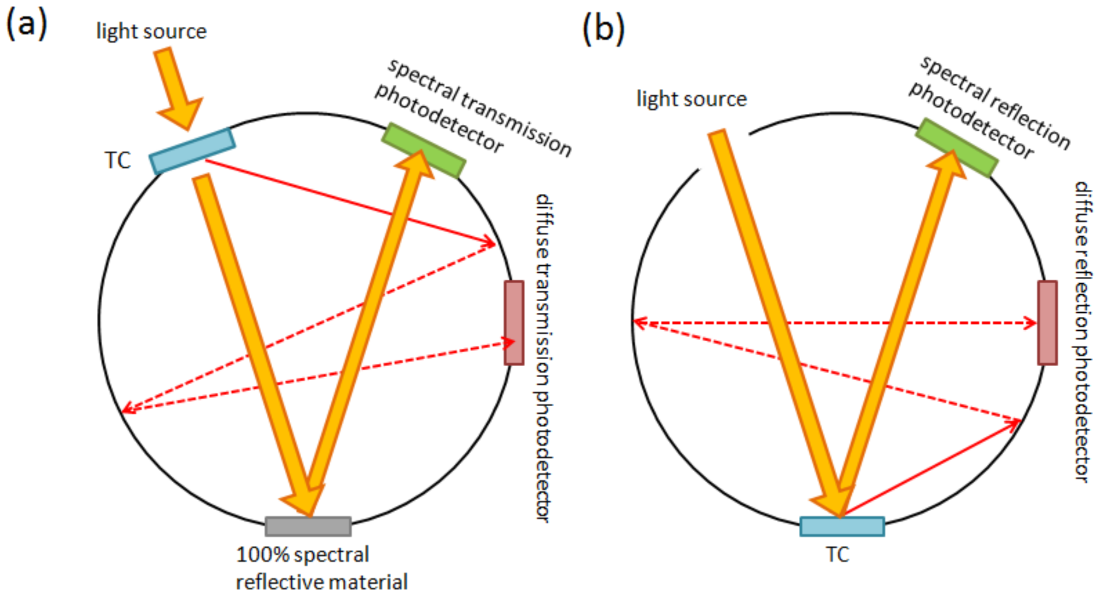

Figure 4.2: (a) Diagram of TC transmission measurement using an integrating sphere. The light source enters the integrating sphere through the TC, resulting in both diffuse transmission (red arrows) and specular transmission (orange arrows). Specularly transmitted photons are reflected from a 100% specular reflective material and detected at the green photodetector. Photons transmitted diffusely are internally reflected by the sphere walls until they are received by the red photodetector (B) Diagram of TC reflectance measurement using an integrating sphere. The light source enters the integrating sphere uninhibited until it strikes the TC, where specularly reflected light (orange arrows) is detected by green photodector and scattered photons are eventually detected by the red photodetector.

An integrating sphere is an enclosed sphere with a highly diffusely reflective interior. Two photodetectors are positioned in order to separately acquire distinct diffuse and specular measurements. All specular photons are received by the photodetector positioned at the specular angle from the TC or the 100% reflective sample (for reflection and transmission measurements, respectively). For diffuse measurement, the specular photodetector port is closed and all diffuse photons are repeatedly reflected within the sphere, until they are received at the diffuse transmission/reflection photodetector.[90,91]

A 100% diffusely scattering sample was used for a diffuse reflectance reference for reflectance measurements and an unimpeded light source was used as a reference for 100% transmission. Transmission and reflectance measurements were taken at 10nm intervals for the spectrum of light from 360nm to 740nm.

4.4 MicroXAM

Roughness values of the Ag NW network were assessed using an Omniscan MicroXAM 5000B 3D. The important numerical values measured by this method device are Sp (maximum peak of analysed region) and Sa (arithmetic average of 3D roughness).

This non-contact surface analysis technique is capable of a vertical scan range of 10s of nms to 10mm. A computer equipped with comprehensive software capable of summit and valley analysis can produce graphical representation and numerical data for the scanned sample area.[92] A region of 0.6617 mm^2 was analysed for each examined NW TC.

4.5 Scanning Electron Microscope

A JEOL JSM-840F scanning electron microscope (SEM), equipped with a cold cathode field emission gun, was used to acquire high-resolution images throughout the study at voltages of approximately 5-6kV. Images acquired by SEM were used to assess the average aspect ratio of synthesized Ag NWs, using a sample size of over 200 NWs and ImageJ measurement tools to measure the NW dimensions. Additionally, SEM images of Ag NWs deposited on glass substrates by vacuum filter deposition were used to enhance TC quality evaluation using percolation theory.

4.6 Solar Simulator

A Keithley Source Meter 2400 was used to supply a range of voltages from -0.5V to 1.5V and measure the corresponding photocurrent over a 61-step sweep during solar simulator testing using a 1.5AM lamp. LabVIEW software was used to program desired input variables, record the applied voltage values, and corresponding photocurrent values for each of the cells tested. All samples were tested under N_2 flow. In addition to testing with the solar simulator, dark measurements were taken to establish the J_o values of the cells. Along with evaluating the V_{oc}, J_{sc}, FF, and η, the J-V values produced from solar simulation were used in conjunction with Equations 12, 13, and 14 in order to evaluate the cell in greater depth.

4.6.1 UV-PHOTODOPING

Some research groups have found solution-processed ZnO films to have poor electrical conductivity characteristics due to low electron concentration, resulting in poor device rectification.[64] This is in large part caused by charge trap states generated by O_2 adsorption on the ZnO surface. However, exposure to UV light has been found to desorb O_2 and free electrons from the trap sites generate deep-seated holes within the valence band, thus passivating possible electron traps within the film.[93] For this reason, the devices underwent efficiency testing both before and after 20 minutes of UV exposure.

CHAPTER 5 - TRANSPARENT CONDUCTOR CHARACTERISATION

Optimal nanowire transparent conductors (NW TCs) are achieved when NWs form a low density, highly percolated network to produce a high transparency, low sheet resistance film. To achieve this for thin film photovoltaic applications, the following is required:

1. A nanowire ink of well-dispersed, high aspect ratio NWs with minimal insulating polymer coating.
2. A deposition method resulting in a highly percolated, smooth film to minimize short-circuiting pathways via NWs pointing out of plane.

In this chapter, we discuss NW synthesis as well as a transfer printing technique to make NW films suitable for photovoltaic device fabrication, developed in Chapter 3. The electrical and optical properties of these films are linked to the percolation and topography of films and compared to the industry standard TC ITO.

5.1 NANOWIRE SYNTHESIS AND DEPOSITION

The nanowires used for TC fabrication were synthesized using methods reported by by Korte et al.[94]. High purity chemical precursors and solvents were found to be most important to synthesis of reproducible, high aspect ratio NWs, which is desirable because high aspect ratio NWs has been found to enhance NW TC performance.[33] NW diameters varied from 70nm to 265nm, resulting in a mean diameter of 130±16nm (Figure 5.1a). NW length varied from 2.4µm to 49.4µm, resulting in a mean length (L_{avg}) of 13.1±0.7µm (Figure 5.1b).

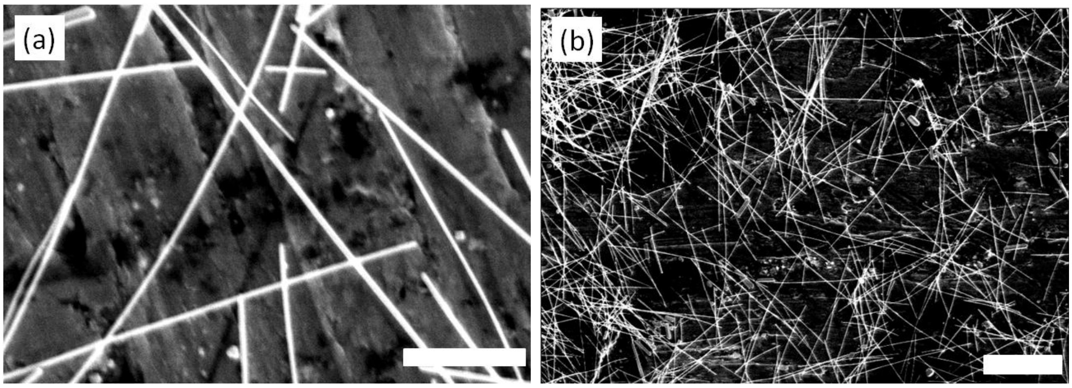

Figure 5.1: SEM images comparing NW diameter size and distribution, 2µm scale bar (a) and NW length, 10µm scale bar (b).

After synthesis, silver nanowire TCs were fabricated by vacuum filter deposition of 200µL, 400µL, 600µL, 800µL, and 1000µL of 0.016wt% Ag NW solution as described in 3.2. By examining NWs before and after deposition, it is found that L_{avg} of deposited NWs increases slightly to 14.6±0.8µm, since most of the NWs of L<10µm fall through the 10µm filter pores upon deposition. However, some NWs L<10µm become entangled with longer NWs, preventing removal by filtration. These shorter NWs, which comprise <20% of deposited NWs, drastically reduce L_{avg} of the deposited NWs. Discounting deposited NWs of <10 µm, L_{avg} of deposited NWs increases from 14.6±0.8µm to 30.0±0.8µm.

It was hypothesized that greater volumes of deposited solution would produce TCs with increased interconnectivity. SEM images of the resulting TCs, shown in Figure 5.2, verify that NW density increases with larger volumes of deposited NW solution. A metric of NW density was determined by measuring the number of NWs per unit area (N), listed in Table 1. NW film thicknesses and topographic properties were measured for each of these NW densities for consideration for later device fabrication and processing.

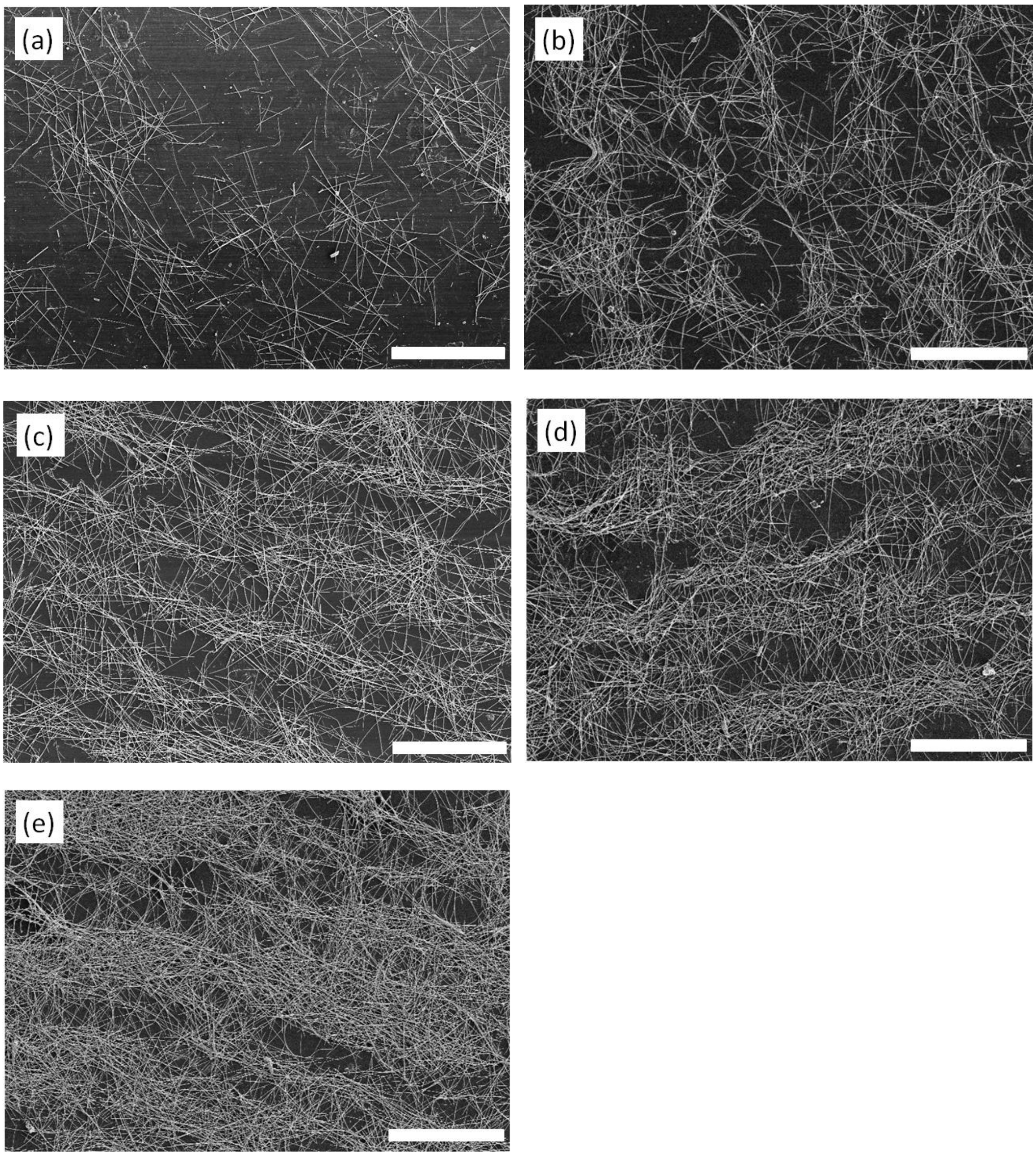

Figure 5.2: (a)-(e) SEM images of vacuum filter deposited Ag NW films, of thicknesses 130nm, 140nm, 160nm, 220nm, and 260nm, respectively. All scale bars are equivalent to 30μm.

5.2 SURFACE PROFILING

5.2.1 Film Height Measurement

The average NW film height was measured using DekTak profilometry. As shown in Figure 5.3, average NW film height increased with greater deposited volumes of NW solution, due to greater frequency of NW overlap and reduced glass exposure. Henceforth, TCs of varying NW densities will be referred to by film height rather than the volume of deposited NW solution. More important than the average film height is the average film roughness and maximum peak height, evaluated using MicroXAM.

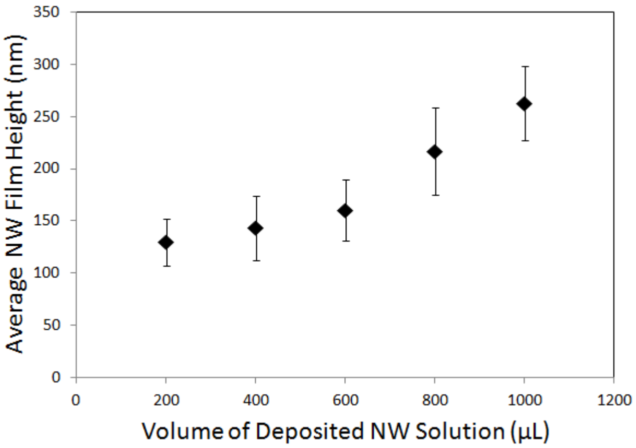

Figure 5.3: Average NW TC film height according to volume of deposited Ag NW solution.

5.2.2 *Surface Roughness Evaluation*

The surface topography of NW TCs was examined using MicroXAM, which has the capability to produce 3-D representations of the profiled sample, shown in Figure 5.4. MicroXAM images were used to confirm that peaks in the z-direction occur at NW overlap sites and areas of high NW density.

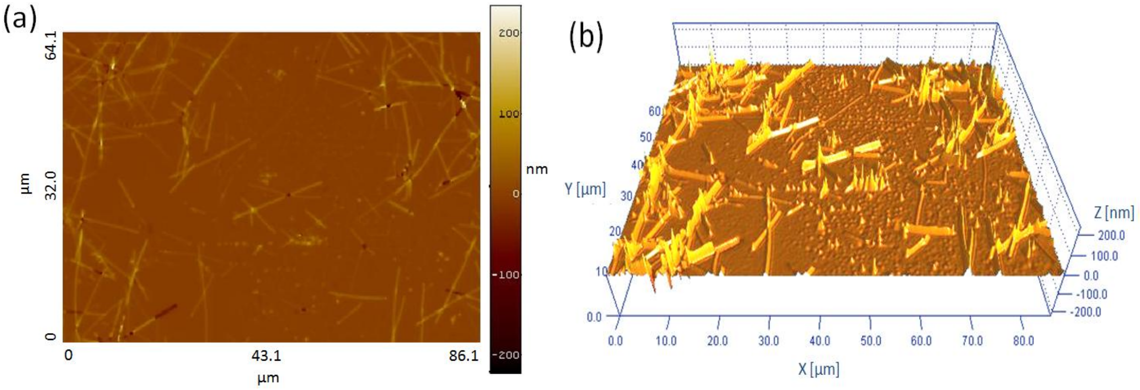

Figure 5.4: MicroXAM images to demonstrate height variations of a low NW-density film (a) 2-dimensionally and (b) topographically.

Average surface roughness (Sa) and maximum peak height (Sp) values must be minimized to prevent short-circuiting during the later stages of device fabrication and processing.[95] It was hypothesized that Sa and Sp values would increase with thicker

NW films, due to greater NW overlap and reduced exposure of comparatively low-roughness glass, shown in Figure 5.2.

Quantitative Sa and Sp data from MicroXAM analysis was extracted and plotted in Figure 5.5. As predicted, both maximum peak height and average surface roughness values increase with NW film thickness. Figure 5.5 demonstrates that thin NW films (<200nm) result in relatively low roughness values (Sa ≤ 25nm) and relatively low maximum peak height (Sp ~400nm). However, the greater Sa and Sp values of thicker NW films caused concern for device fabrication, as a variable substrate topography can enhance cracking and short circuiting.[95,96] After surface profiling was finished, the current-carrying capacity of each of these NW films was measured to evaluate functionality in a solar cell.

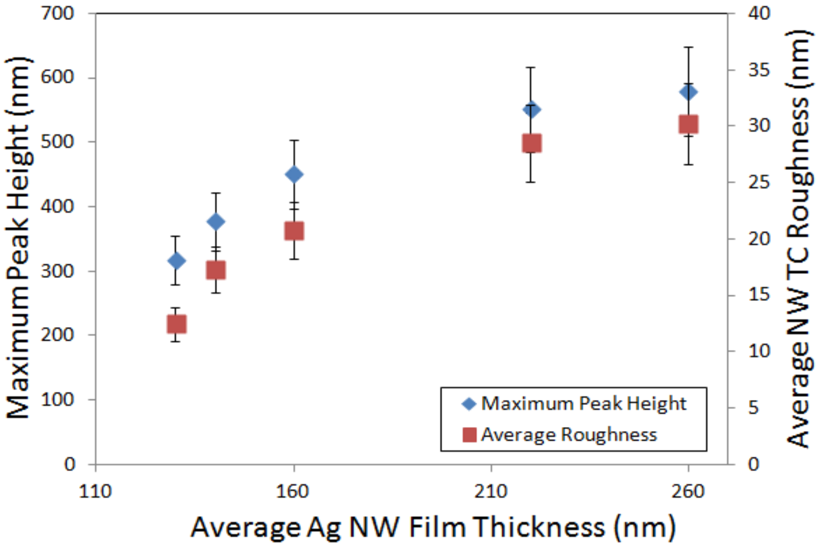

Figure 5.5: Average Ag NW TC roughness and average maximum peak height per 0.66 mm^2 area scanned according to average Ag NW film thickness.

5.3 SHEET RESISTANCE MEASUREMENT

Nanowire film conductivity is dependent upon the number of NW junctions through which a current can flow.[22] Because of this, it was hypothesized that R_{sheet} would decrease as the number of NW junctions increased with NW density. R_{sheet} was expected to plateau after NW films achieved maximum percolation.

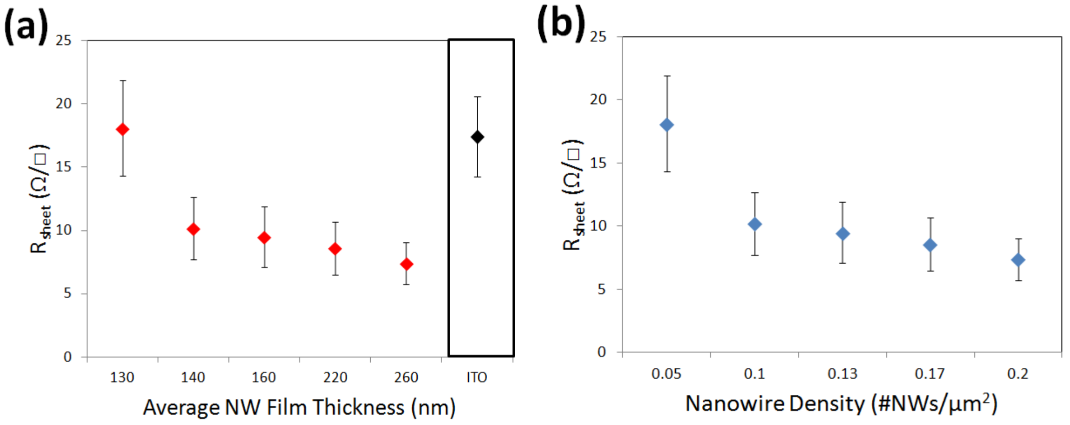

Figure 5.6: Average measured R_{sheet} values of ITO and NW TCs according to NW film (a) thickness and (b) nanowire density.

Four point probe measurements, shown in Figure 5.6, verified both hypothesises, as there is a significant drop in R_{sheet} from the lowest density NW film to NW films >130nm thick, but a more gradual decrease in R_{sheet} reduction for thicker NW films. With the exception of the 130nm NW film, all NW films yielded R_{sheet} values less than that of ITO. These measurements were then compared to calculated R_{sheet} values using percolation theory.

5.4 PERCOLATION

As discussed in 2.1.4.1, the interconnectivity of NWs plays a vital role in determining the current-carrying capacity of the TC. The critical NW density to facilitate percolation, N_c, was evaluated using Equations 4 and 5, where L=14.6±0.8µm (L_{avg} of vacuum filter deposited Ag NWs, from 5.1), yielding

N_c=.027±0.003 NWs/ μm^2. For each NW film thickness, Table 1lists the evaluated N-values, the calculated R_{sheet} values using a dimension value α=1.42,[30] and the R_{sheet} values from the previous section. It is evident that there is some source of error in the application of the percolation equation, due to the fact that the calculated R_{sheet} is up to an order of magnitude greater than the measured R_{sheet} value.

NW Film Thickness	**Measured N-value (#NW/μm^2)**	**Calculated R_{sheet} (Ω/sq)** *L_{avg}=14.6μm*	**Calculated R_{sheet} (Ω/sq)** *L_{avg}=30.0μm*	**Calculated R_{sheet} (Ω/sq)** *α=1.33*	**Measured R_{sheet} (Ω/sq)**
130nm	0.05	180.0	65.3	50.1	18 ± 3.8
140nm	0.10	39.2	25.4	20.7	10 ± 2.5
160nm	0.13	24.3	17.6	14.7	9 ± 2.4
220nm	0.17	16.3	12.7	10.8	8 ± 2.1
260mm	0.20	12.5	10.1	8.7	7 ± 1.7

Table 1: NW density (N), calculated R_{sheet} values and measured R_{sheet} values for varying NW densities.

One source of error are the minority NWs of L<10μm which become entangled with longer NWs and significantly reduce L_{avg}, despite the fact that they comprise <20% of the total number of NWs. This error was reduced by recalculating R_{sheet} using L_{avg}=30.0±0.8μm, mentioned in 5.1, in Equation 5. Once recalculated, N_c=6.4x10^{-5}±4x10^{-7} NWs/ μm^2 and the resulting R_{sheet} values were less than an order of magnitude from the measured values (Table 1). The calculation can be further improved by using the 2-dimensional percolation exponent α=1.33 in Equation 4 (Table 1).

After the electrical properties of the NW TCs were measured and calculated by four point probe and percolation theory, respectively, the optical properties of the NW films were evaluated using an integrating sphere.

5.5 TRANSMISSION AND REFLECTION EVALUATION

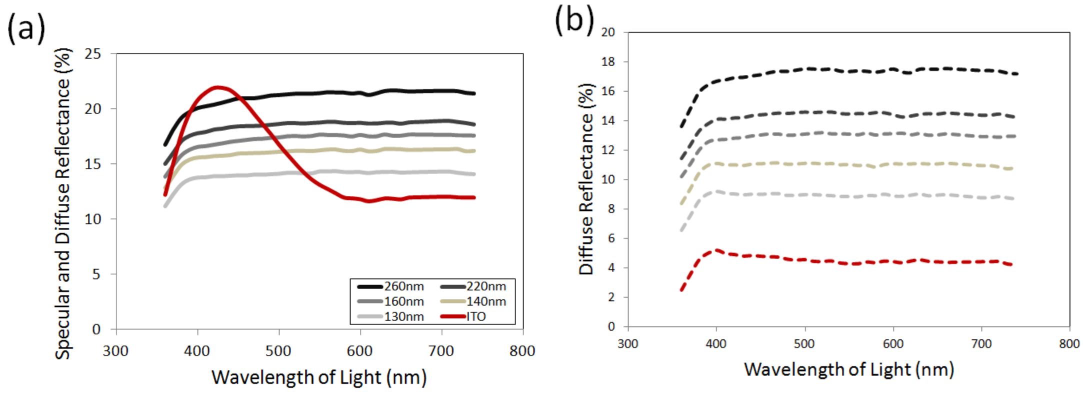

Figure 5.7: (a) Percentage of incident light which is reflected specularly or diffusely (solid lines) for ITO (red) and varying Ag NW film thicknesses (shades of grey). (b) Dashed lines correspond to percentage of incident light reflected diffusely. Colours of dashed line synonymous with TC samples of (a) and Figure 5.8.

Previous reports of Ag NW TCs have reported reflection as a major problem for light transmission through NW TCs caused by both specular and diffuse reflection.[14,97,16] Because of this, specular and diffuse reflectance was measured separately using an integrating sphere. These measurements, graphed in Figure 5.7, show that NW film reflection is dominated by scattering, while ITO reflection is dominated by specular reflection.

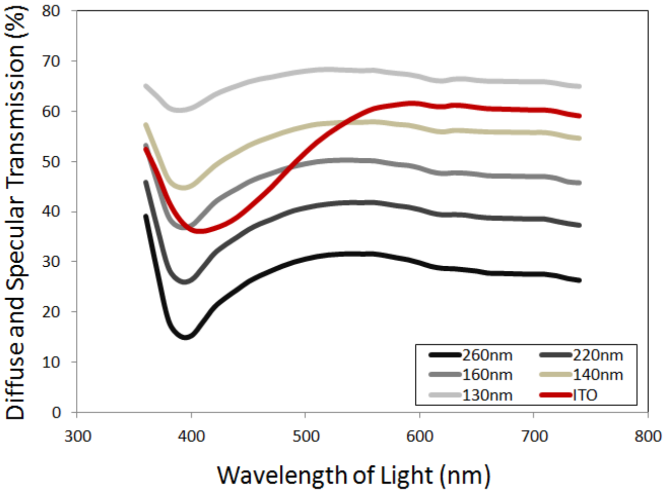

Figure 5.8: Combined specular and diffuse transmission for ITO (red) and varied Ag NW film thickness (shades of gray).

Combined specular and diffuse transmission measurements are shown in Figure 5.8. As expected, thin NW films result in higher transmission. Despite the negative consequences of scattering in reflectance mode, diffuse transmittance can substantially enhance solar cell performance due to greater optical path length.[16] Furthermore, ITO is susceptible to photonic absorption of the ultraviolet to blue spectrum. This photonic absorption accounts for the reduced transmission of low-reflectivity ITO films.[98] Visible light which is not scattered or directly transmitted by Ag NW films may disturb unbound electrons of individual nanowires from their original position, generating collectively propagating electromagnetic waves down the length of the nanowire, which was previously mentioned in Chapter 2. These propagating electromagnetic waves, known as plasmons, have been shown to reemit absorbed light, thus allowing for reduced absorption and greater light transmission into the cell.[99]

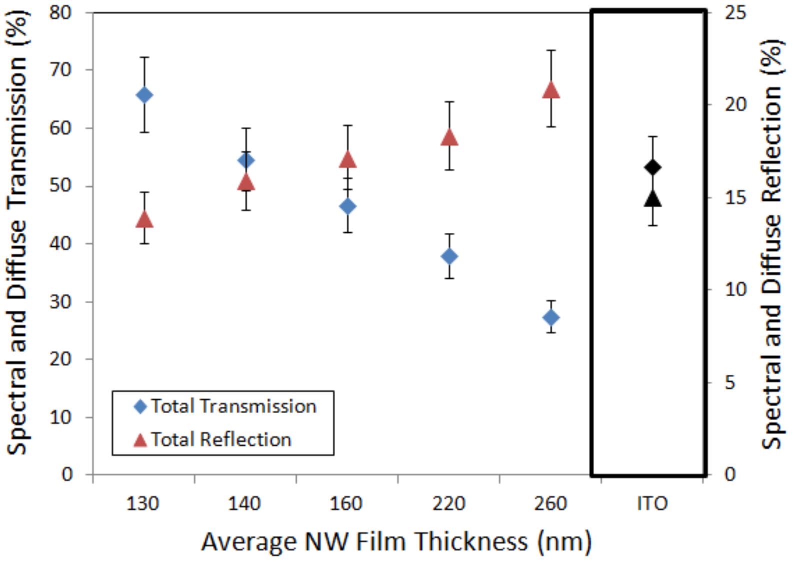

Figure 5.9: Specular and diffuse transmission and reflectance of Ag NW TCs of varying film thickness.

Absolute average transmission and reflectance values are plotted as a function of NW film thickness in Figure 5.9. Transmission is maximized and reflection is minimized for films 140nm-160nm thick. These averaged values are used in the next section to calculate the ratio of conductivity to absorbance $(\frac{\sigma}{\alpha})$ using Equation 3 to act as figure of merit which balance optical and electronic properties.

5.6 CONCLUSION

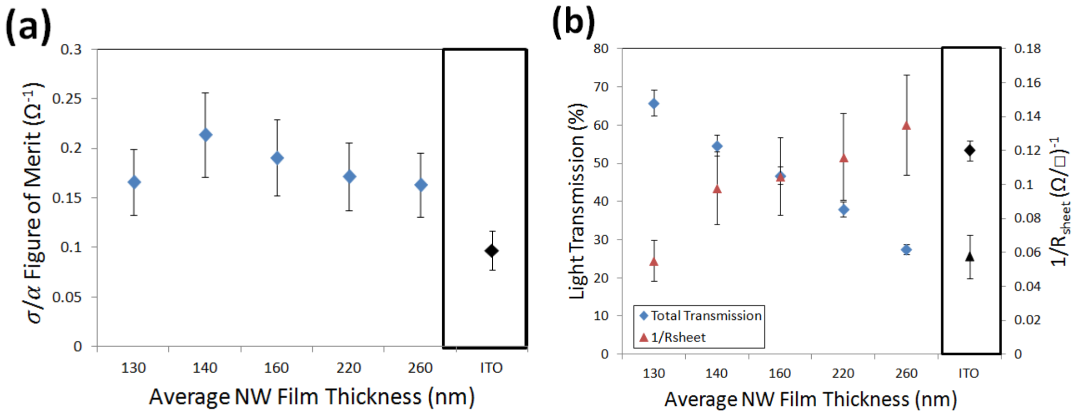

Figure 5.10: TC evaluation according to (a) Figure of merit $\frac{\sigma}{\alpha}$, determined by Equation 3, where greater $\frac{\sigma}{\alpha}$ values correspond to higher quality TCs and (b) average transmission and sheet conductivity.

Data from earlier in this chapter is now synthesized to determine which of the NW films will provide the best transparent conductor for solar cell fabrication. Calculated $\frac{\sigma}{\alpha}$ values and TC transmission versus conductivity are plotted as a function of NW film thickness in Figure 5.10a and 5.10b, respectively. Both methods eliminate the highest and lowest NW film thicknesses due to low transparency of thick NW films and high R_{sheet} of the thinnest NW film. Therefore, 160nm NW films were selected for preliminary device fabrication, described in the next chapter.

CHAPTER 6 - DEVICE CHARACTERIZATION

Once the Ag NW synthesis and deposition methods were optimised to consistently produce TCs with good optical and electronic properties, the first trial of Ag NW-PbS QD solar cell fabrication was attempted. Figure 6.1 represents the energy band diagram of these devices.[100-102,103] For this device, PbS acts as the p-type material and ZnO acts as the n-type material and is expected to act as a p-n junction as described in 2.3.5.[81]

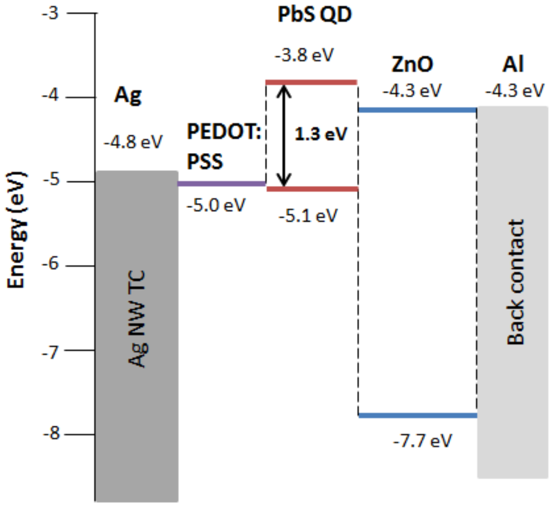

Figure 6.1: Energy band structure of Ag NW-PbS QD solar cell.

Once excitons are generated in the PbS photoactive layer, PEDOT:PSS transfers holes from the photoactive layer to the NW TC.[64] ZnO acts as the large band gap heterojunction layer, removing photogenerated, high-energy electrons and simultaneously acting as a blocking layer for holes attempting to migrate to the Al contact, described in 2.3.4.[72] ITO devices of this structure produce V_{oc} values and J_{sc} values ranging from 0.45-0.55V and 2-10mA/cm^2, respectively.[103]

Careful consideration of this energy structure was required to comprehend data obtained by device testing and to attempt to enhance device performance. The following chapter examines deposition of each layer and develops a processing strategy to make functioning devices as well as understanding the nature of charge transport and opportunities for device improvement.

6.1 Short Circuiting Reduction

From early stages of research, it became apparent that device short-circuiting was the greatest hurdle to the fabrication of functional solar cell with a NW TC. Preliminary devices were fabricated by sequentially spin-coating PEDOT:PSS, PbS, and ZnO, as described in 3.3. These initial devices failed due to short-circuiting devices, as indicated by very low measured R_{shunt} values and a linear increase in current with applied voltage shown in Figure 6.2.

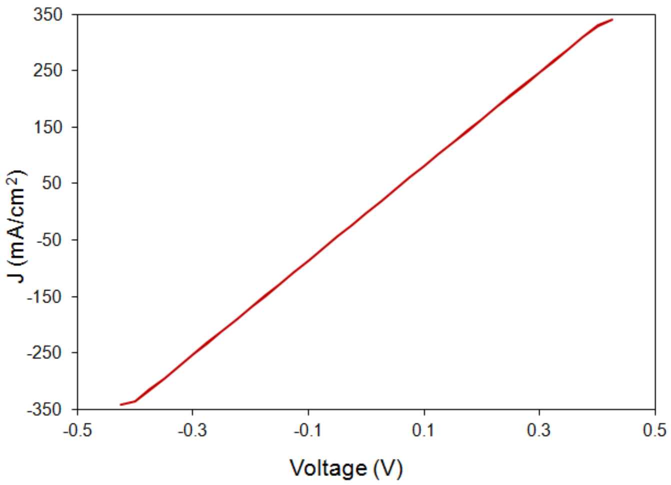

Figure 6.2: J-V plot of a short-circuiting device. Equation for this plot can be represented by the standard equation V=IR, where R corresponds to the slope of the line and the resistivity of the short-circuiting junction.

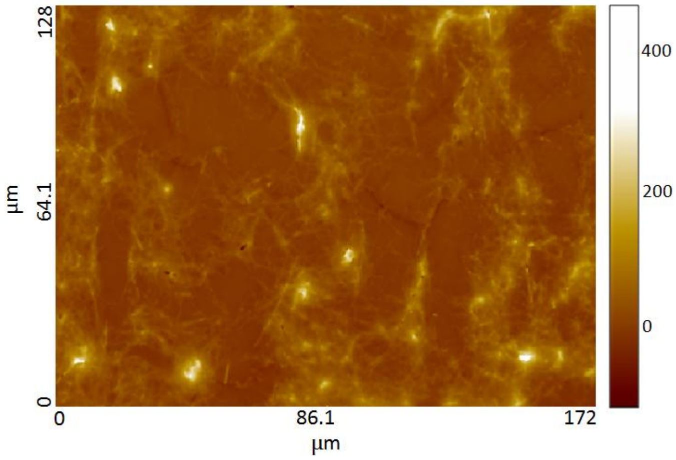

Figure 6.3: MicroXAM image of device where NWs are visible despite subsequent layers of PEDOT:PSS, PbS QDs, and ZnO.

MicroXAM examination of devices revealed that NWs were still visible after device fabrication, as shown in Figure 6.3. This observation heightened concern that penetration of NWs through subsequent layers to the aluminium cathode may be the cause of device short-circuiting. MicroXAM also revealed high levels of cracking in the PbS film which could provide another source of short-circuiting, as shown in Figure 6.4 in the following section.

Some degree of PbS film cracking is inevitable due to the film volume change caused by the exchange of long oleic acid synthesis ligands for shorter EDT ligands used in device fabrication,[65] yet it is possible that the roughness of the NW TC could exacerbate this problem. Establishing possible methods of remediating short-circuiting became the first priority, beginning with modification of the ZnO layer to minimise anode-cathode shorts and the detrimental effects of cracks in the PbS film.

6.1.1 ZNO LAYER IMPROVEMENT

The ZnO layer was selected to modify first because it is the thickest layer of those deposited in the original device structure, thus has a greater possibility of encapsulating penetrating NWs. Additionally, because it is the barrier between cracked PbS films and Al, it is the only variable which can be altered after PbS deposition in order to potentially fill cracks and reduce crack-induced short-circuiting.

Although ZnO is n-doped, ZnO is a wide band-gap semiconductor, thus far less conductive than Al. It is optimal for NWs to never penetrate the PEDOT:PSS layer, however, encapsulation of the Ag NWs in ZnO is far less detrimental to device-performance than is the penetration of the NWs to Al. It was believed that short-circuiting could be negated by increased ZnO thickness as well as improved ZnO adhesion to the PbS film and penetrating NWs. Therefore, both of these methods of ZnO layer enhancement were explored.

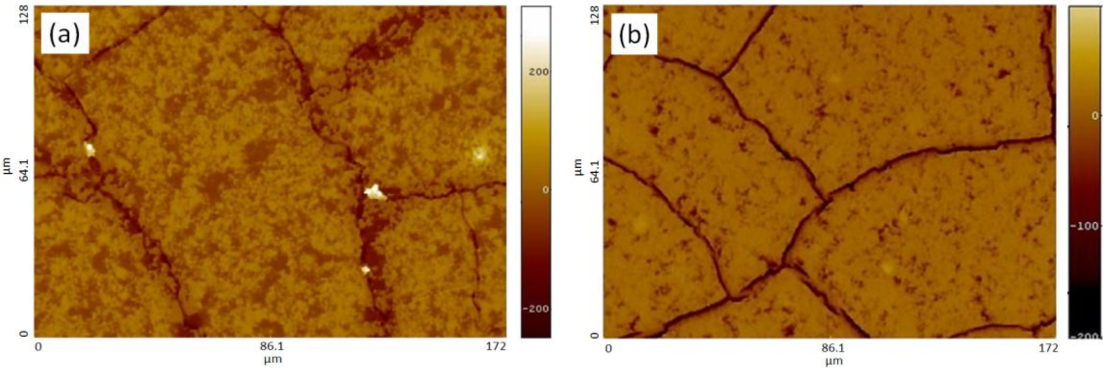

Figure 6.4: (a) Device without plasma treatment before ZnO deposition has greater roughness (Sa=30.8nm) and less conformal ZnO coverage compared to (b) device with 15sec H_2/N_2 treatment before ZnO (Sa=14.4nm). The dark orange, cracked layer is the PbS layer, whereas the yellow/ light orange film corresponds to the subsequently deposited ZnO film.

Plasma treatments are known for increasing surface energy in order to promote adhesion and conformal coating of surfaces.[104] A 15sec H_2/N_2 plasma treatment immediately after PbS deposition, before ZnO deposition, was used to enhance ZnO filling of the cracks in the PbS layer and increase ZnO coverage of penetrating NWs. MicroXAM images of a sample without and with plasma treatment before ZnO deposition (Figure 6.4a and 6.4b, respectively), confirmed that plasma treatment increases ZnO film uniformity.

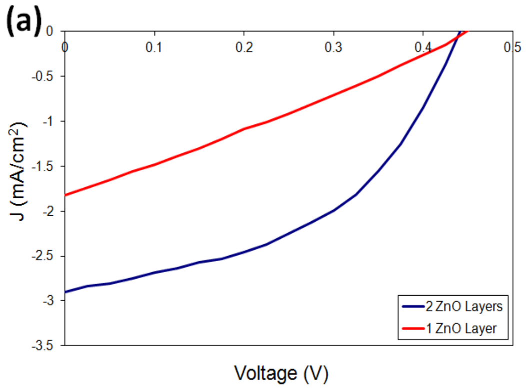

(b)

	1 ZnO Layer	2 ZnO Layers
J_{sc} (mA/cm²)	1.8 ± 0.3	2.9 ± 0.2
V_{oc} (V)	0.45 ± 0.1	0.44 ± 0.01
PCE (%)	0.18% ± 0.06%	0.602% ± 0.005%
R_{shunt} (Ω-cm²)	1200 ± 300	4500 ± 100
J_o (μA/cm²)	3 ± 1	1 ± 0.3
Diode Ideality Factor (n)	3.5	3.0

Figure 6.5: (a) J-V curves of devices with 1 and 2 layers of ZnO deposited after H_2/N_2 plasma treatment and (b) performance metrics of devices with 1 and 2 layers of ZnO.

Numerically, MicroXAM analysis proved that plasma treatment before ZnO deposition reduced the surface roughness by approximately 50% compared to device fabrication without plasma treatment, resulting in the first functioning solar cell demonstrated by the J-V curve in Figure 6.5a. The low V_{oc}, J_{sc} and PCE values (1.9 mA/cm^2, 0.21V and 0.18%, respectively) left much room for device improvement.

After ZnO adhesion was improved with plasma treatment, device performance enhancement was attempted with another H_2/N_2 plasma treatment and deposition of a second ZnO layer at a slightly higher spin speed (2000rpm). J_{sc} and PCE values increased substantially with this additional ZnO layer, as shown in Figure 6.5. R_{shunt} values increased over 100% with an additional layer of ZnO, consequently leading to a decrease in I_o from 3 ± 1 μA (1 layer ZnO) to 1 ± 0.3 μA/cm^2 (2 layers ZnO) and a decrease in the diode ideality factor (n) from 3.5 to 3.0 for fitting dark I-V curves to Equation 14, shown in Figure 6.6.

Because plasma treatment prior to deposition of two ZnO layers successfully reduced short-circuiting to produce the first functioning Ag NW-based PbS QD devices, this became standard practice for device fabrication. Although this ZnO modification eliminated short-circuiting for many devices, short-circuiting remediation was also attempted using a hypothesis that passing a large current density through a small number of NW-Al junctions could destroy those short-circuiting pathways.

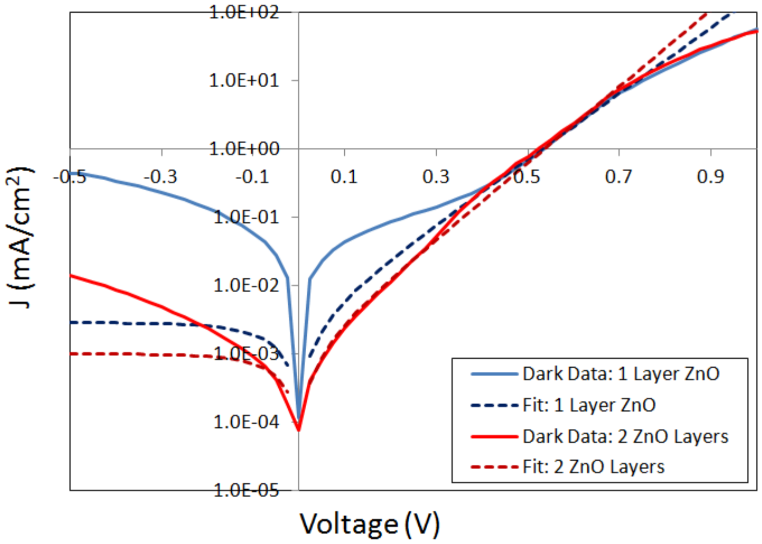

Figure 6.6: Dark current measurements of devices with 1 and 2 layers of ZnO and fitted Equation 14 for J_o and *n* value estimation.

6.1.2 EFFECTS OF JOULE HEATING

Khalig et al. proved that large current densities passed through an Ag NW network can result in NW breakup due to joule heating, inevitably leading to a discontinuous current pathway.[105] Because of this, some short-circuiting devices underwent multiple voltage sweeps from -0.5V to 1.0V in an attempt to destroy NW-Al contact short pathways.

Figure 6.7a and 6.7b show a drastic change in J-V behavior under multiple -0.5V to 1.0V voltage sweeps of a device under solar illumination. The solar cell progressed from a completely short-circuiting device with a R_{shunt} value of 10 Ω-cm^2 upon the first voltage sweep to a rectifying device with an increase in R_{shunt} by almost two orders of magnitude upon the second voltage sweep.

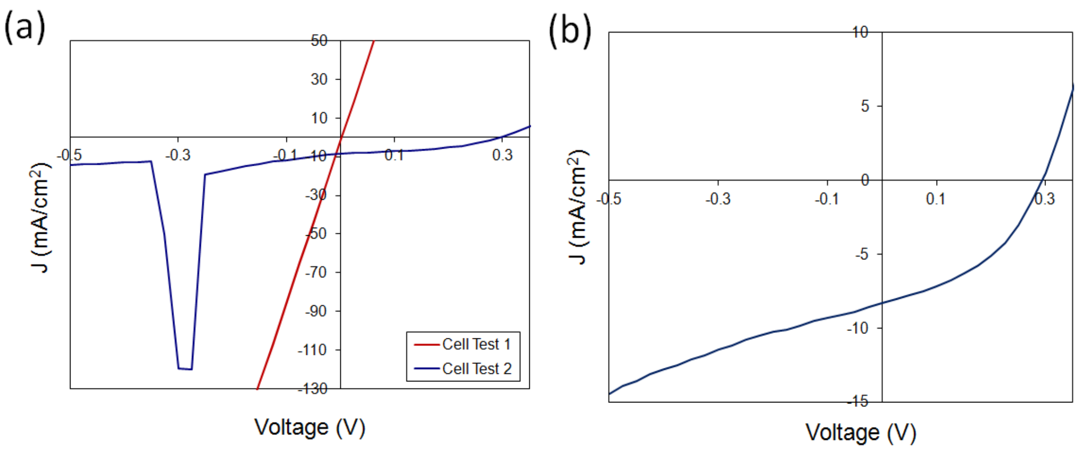

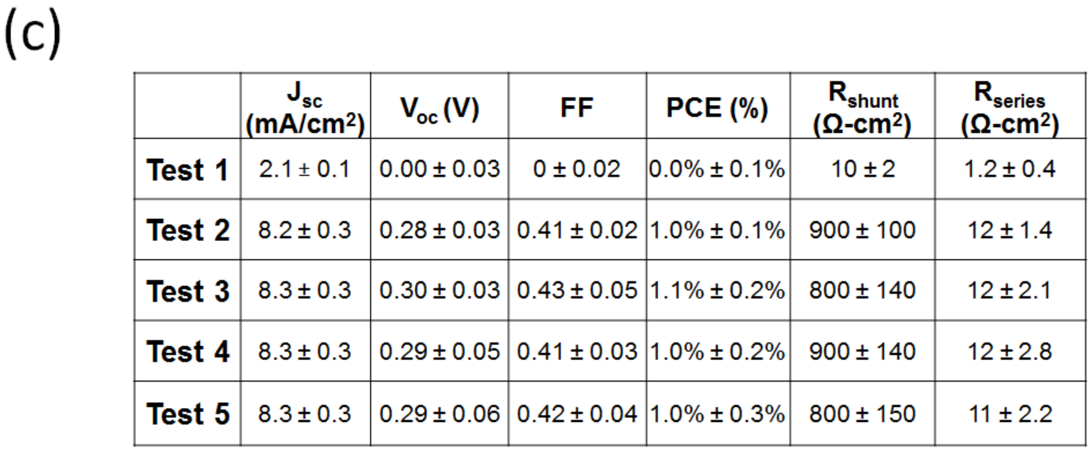

	J_{sc} (mA/cm^2)	V_{oc} (V)	FF	PCE (%)	R_{shunt} (Ω-cm^2)	R_{series} (Ω-cm^2)
Test 1	2.1 ± 0.1	0.00 ± 0.03	0 ± 0.02	0.0% ± 0.1%	10 ± 2	1.2 ± 0.4
Test 2	8.2 ± 0.3	0.28 ± 0.03	0.41 ± 0.02	1.0% ± 0.1%	900 ± 100	12 ± 1.4
Test 3	8.3 ± 0.3	0.30 ± 0.03	0.43 ± 0.05	1.1% ± 0.2%	800 ± 140	12 ± 2.1
Test 4	8.3 ± 0.3	0.29 ± 0.05	0.41 ± 0.03	1.0% ± 0.2%	900 ± 140	12 ± 2.8
Test 5	8.3 ± 0.3	0.29 ± 0.06	0.42 ± 0.04	1.0% ± 0.3%	800 ± 150	11 ± 2.2

Figure 6.7: (a) Improved device performance from the first -0.5V to 1.0V voltage application ("Cell Test 1") to the second -.5V to 1V voltage application ("Cell Test 2"), where the dramatic dip in current density at -0.3V indicates the breakup of NWs in contact with the Al electrode. (b) A J-V curve of the same device on the 3rd -0.5V to 1.0V voltage sweep of the device, demonstrating unhindered device rectification. Continuous device testing resulted in slightly improved J_{sc} values with the caveat of reduced V_{oc} and PCE values (c).

There is a sharp dip in current density at approximately -0.3V of the second voltage sweep which was previously observed by Khaligh et al. during stages of Ag NW breakup.[105] Following this sharp J-V dip, a non-linear J-V curve emerges, implying a functioning rectifying device. On the third voltage sweep (Figure 6.7b), the device shows no sign of short-circuiting and the device parameters plateau (Figure 6.7c).

Although joule heating can be beneficial in destroying undesirable NW-Al pathways, increasing the device temperature may have detrimental side effects, such as unintended QD growth, increased R_{series} values by NW breakup in the Ag NW TC, or increased ZnO conductivity between NW-Al electrodes, resulting in lower R_{shunt} values.[76,105,106] For these reasons, short-circuiting reduction was investigated by modifying the electronic properties of ZnO.

6.1.3 TIME-DEPENDENT DEVICE PERFORMANCE

The final mechanism of shunt pathway reduction was realized after a short aging effect. Cells showed improvement with brief device-aging when stored in an N_2 environment, shown in Figure 6.8. Although the J_{sc} and R_{series} values varied very little, device V_{oc} and R_{shunt} values increased by almost 100%.

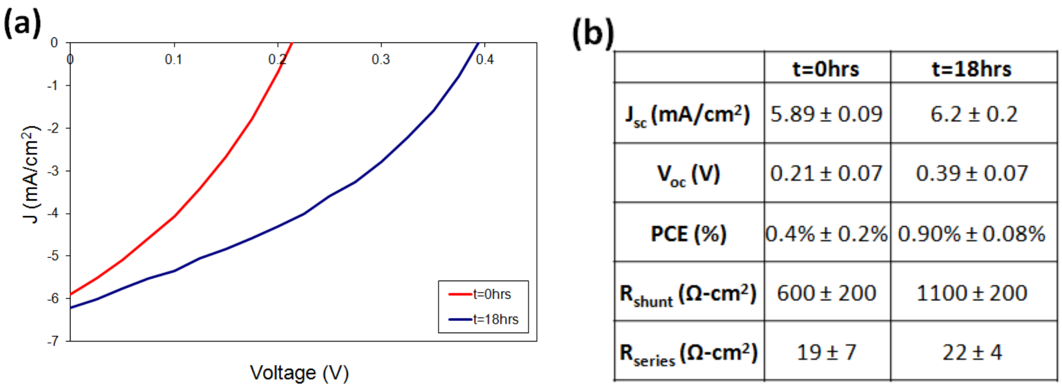

	t=0hrs	t=18hrs
J_{sc} (mA/cm^2)	5.89 ± 0.09	6.2 ± 0.2
V_{oc} (V)	0.21 ± 0.07	0.39 ± 0.07
PCE (%)	0.4% ± 0.2%	0.90% ± 0.08%
R_{shunt} (Ω-cm^2)	600 ± 200	1100 ± 200
R_{series} (Ω-cm^2)	19 ± 7	22 ± 4

Figure 6.8: (a) Device J-V plot before and after 18hr aging in N_2 environment and (b) performance metrics of device before and after aging (t= 0hrs and t= 18hrs, respectively).

The increase in R_{shunt} indicates that aging causes either a change in NW shorting or bulk material properties. Because no other variables are introduced between solar simulation testing, the changes likely occur at the atomic level in order to reduce free energy of the system. Two plausible theories are offered to explain this phenomenon, which may operate together or independently, shown in Figure 6.9.

1. Ag atomic migration and subsequent doping of the ZnO layer.
2. Diffusion of oxygen from the ZnO to the penetrating NW, forming an Ag_xO_y shell.

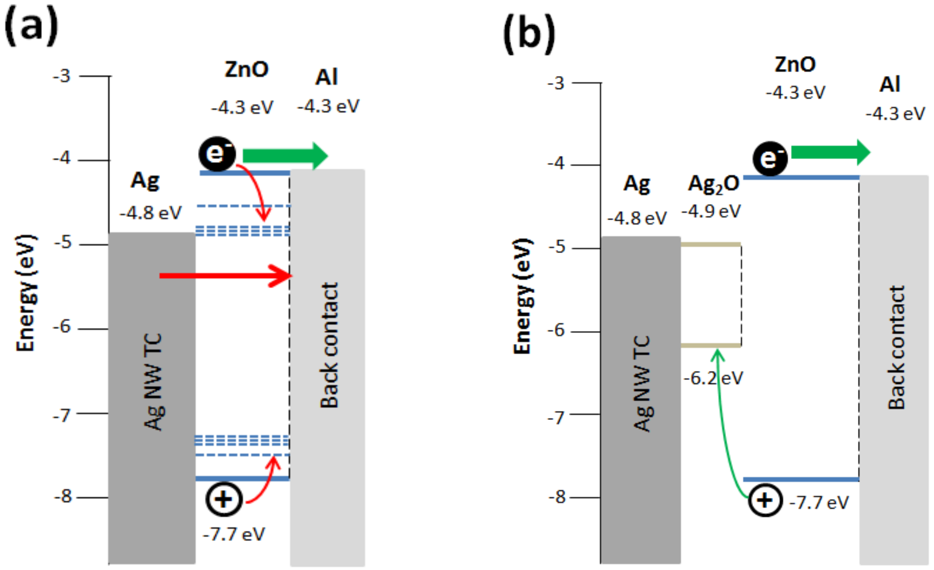

Figure 6.9: (a) Devices before aging, red arrows reflect undesired carrier pathways and green arrows represent desired carrier pathways. Current leakage can occur via recombination in ZnO defect regions (shaded blue regions), tunnelling of electrons from NWs through thin ZnO barriers or direct contact of ZnO-Al electrodes (thick red arrow). (b) Proposed beneficial effects of aging: development of Ag_2O shell around penetrating Ag NWs and removal of defect sites in ZnO due to Ag-doping and UV-doping increases height and width of energy barrier between Ag and Al, reducing current leakage.

Although ZnO is an n-type semiconductor, ZnO can be Ag-doped to become a p-type semiconductor, due to substitutional doping of Ag at Zn sites.[107] However, this requires very high temperatures for thermal energy to engage Ag diffusion. It has been observed that at low temperatures (<175°C), such as those supplied by joule heating of Ag NWs,[105] Ag atoms do not have the kinetic energy to displace Zn atoms from their inherent lattice sites.[107] Instead, oxygen atoms or Ag_2O molecules can passivate defects, removing defect sites within the ZnO band gap, thus resulting in a semi-insulative ZnO film.[108] Due to poor diffusion of Ag atoms, these semi-insulative portions of ZnO could concentrate at sites of NW penetration through the PbS layers, reducing current leakage from the NWs but conserving the n-type conductivity of ZnO away from NW-ZnO junction regions.

Alternately, the formation of an Ag_xO_y shell could occur when O_2 is desorbed from the ZnO film during both UV-photodoping and heat treatment caused by joule heating.[109] According to Schmidt et al., Ag_xO_y forms when free O_2 molecules are physisorbed and subsequently chemisorbed to the Ag NW surface, due to electron transfer from Ag to the O_2 antibonding π^* orbital.[110] As the concentration of O_2 molecules on the Ag NW surface increases, the Ag lattice is restructured in order to generate an Ag_xO_y shell. Because the resistivity of silver oxides are over ten orders of magnitude greater than that of Ag,[111] shunt pathways could be reduced by Ag_xO_y shell formation, resulting in improved device performance, shown in Figure 6.9.[100-102]

Despite this slight improvement with aging, devices are still susceptible to QD degradation, causing a reduction of both J_{SC} and V_{oc} >48hrs after device fabrication.[112]

The combination of methods outlined in this section successfully overcame the initial device short-circuiting issue. NW film thickness was then varied in an attempt to further improve PCE.

6.2 Effects of Nanowire Density

A study of the effect of NW density on device performance was undertaken using the NW TC samples tested in Chapter 5. It was hypothesized that an optimal Ag NW film thickness exists which combines the benefits of good electrical conductivity and transparency with quality NW distribution and surface area. This enables charge carrier generation to be as close as possible to collection sites at the NW electrode.

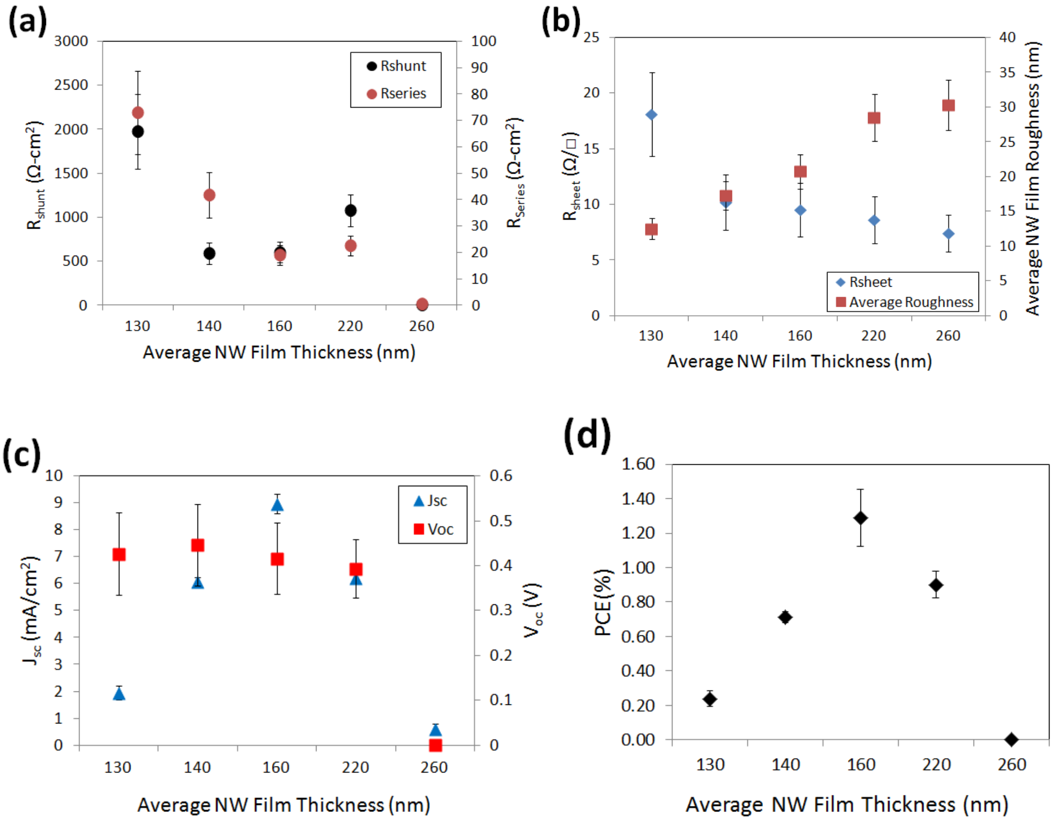

Figure 6.10: (a) R_{series} and R_{shunt}, (b) R_{sheet} and average Ag NW roughness (Sa), (c) J_{sc} and V_{oc}, (d) and PCE values for devices of varying Ag NW thickness.

Figure 6.10a shows that thicker Ag NW films result in lower R_{series}, which follows the trend of reduced R_{sheet} results with greater Ag NW film thickness noted in Chapter 5. Although low R_{series} devices typically result in high J_{sc} devices, denser Ag

NW films result in higher roughness films, shown in Figure 6.10b. It is proposed that higher density NW films lead to increased cracking of later-deposited films, resulting in greater short-circuiting. As noted in 5.4, higher density NW films also result in greater maximum peak heights, providing additional paths for short-circuiting. Greater shunt pathways with increased NW density correlates to reduced R_{shunt} and V_{oc} values, as shown in Figure 6.10a and 6.10c, respectively. Figure 6.10d indicates that this V_{oc}-J_{sc} trade-off results in an optimal PCE for Ag NW TCs with an average thickness of 160nm and a completely short-circuited device for Ag NW TCs >260nm thick.

Using these results, the next step was to optimise the PbS layer thickness.

6.3 Impacts of Quantum Dot Layer Thickness

Previous research has indicated that the optimal PbS thickness is equivalent to the depletion width plus the diffusion length of an exciton, thus excitons generated within this region can drift or diffuse efficiently for charge separation at the ZnO-PbS junction. Willis et al. demonstrated that J_{sc} decreases by more than 50% for a film 150nm greater than the optimal thickness [103]. This is because devices fabricated

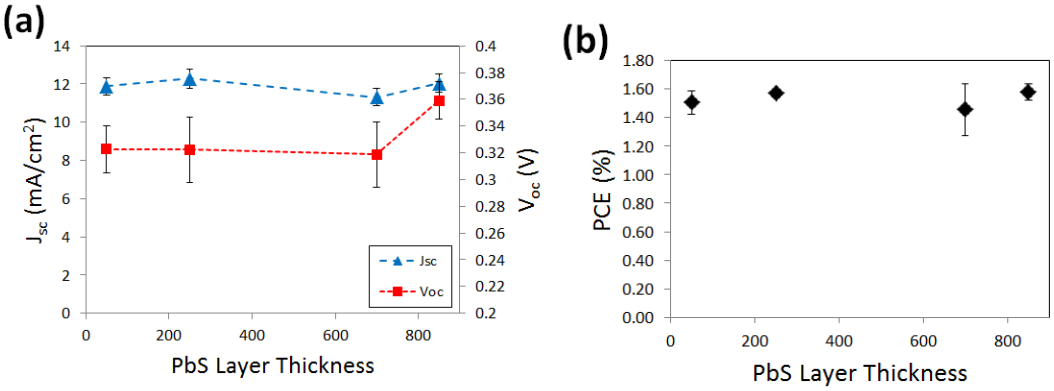

Figure 6.11: (a) J_{sc} and V_{oc} and (b) PCE values for devices of varying PbS layers

with a PbS film greater than the optimal PbS thickness results in charge carrier recombination before reaching the ZnO-PbS interface [71]. Based upon this past experimental investigation, a similar result was expected for Ag NW devices with PbS films between 50 and 850nm.

Figure 6.11a and 6.11b show that there is very little difference in J_{sc} and PCE with changing PbS thickness, while only V_{oc} increases significantly for the thickest device. The V_{oc} increase for the thickest film is most likely caused by reduced shunt pathways by greater NW encapsulation. The stagnant J_{sc} and PCE values are contrary to the findings of Willis et al. who found a 50 nm thick PbS layer maximized J_{sc} and PCE, with decreasing device performance with greater PbS thickness.

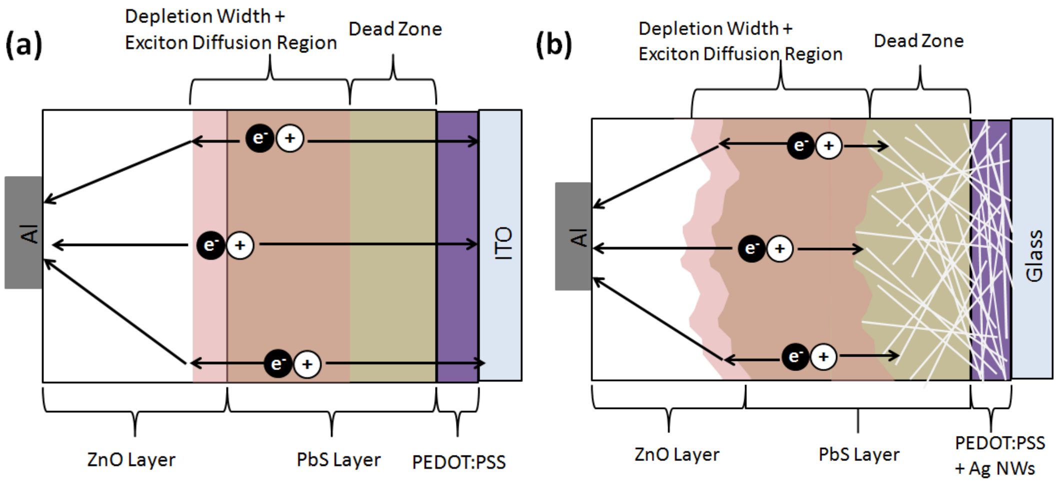

Figure 6.12: (a) Typical charge extraction of a QD solar cell functioning as a p-n junction. Excitons generated beyond an exciton diffusion length of the depletion width cannot be collected for photocurrent. (b) Speculated charge extraction Ag NW- PbS QD solar cell. Charge extraction enhancements caused by high ZnO-PbS interface area due to NW substrate roughness and excitonic uptake of holes by penetrating NWs.

The unchanging J_{sc} and PCE values for the increased PbS film thickness could be due to variation in the PbS-ZnO interface caused by penetrating NW. High-roughness NW films could produce a greater PbS-ZnO interface area for enhanced charge separation (Figure 6.12b) compared to a device fabricated using a low-roughness ITO TC (Figure 6.12a). This explanation for device enhancement is supported by other high surface area bulk heterojunctions, which have been shown to increase J_{sc} and PCE.[79] Overall, the data for the PbS thickness suggests that the devices are not yet at their optimal thickness and could be made thicker.

Further investigation of the relationship between PbS thickness and device performance is necessary in order to validate either theory. Plans for future work with PbS film thickness and other aspects of these devices is discussed in the next chapter.

CHAPTER 7 - CONCLUSIONS AND FURTHER WORK

7.1 Conclusions

This study evolved from basic nanowire synthesis and deposition optimization to the fabrication of the first reported PbS quantum dot solar cell using a silver nanowire transparent conductor (Ag NW TC). Nanowire films were deposited by a vacuum filter stamping process which removed low-aspect ratio NWs in order to improve film transparency and reduce film roughness.

The greatest obstacle to the fabrication of quality devices was short-circuiting pathways caused by high-roughness NW films and NW penetration to the opposing electrode. The following methods have been found to be the most successful means of reducing shunt pathways:

1. Fabrication of devices using medium-density NW films (thickness less than 200nm). These films pair high sheet conductivity with minimal film roughness to optimise cell J_{sc} and V_{oc}, respectively.
2. Enhancement of the ZnO layer by plasma treatment and deposition of multiple layers of ZnO. These processes improve coating of penetrating nanowires and cracks in the PbS film, which otherwise act as sources for leakage current.
3. Aging devices in an N_2 environment for 18 hours after UV photodoping. It is proposed that this process reduces shunt pathways by either Ag-doping of the

ZnO film or formation of an insulative Ag_xO_y shell around penetrating nanowires.

4. Increased PbS film thickness, which provides improved encapsulation of penetrating nanowires to reduce leakage current.

A combination of these methods achieved a champion cell with conversion efficiency of 2.2% ± 0.2%.

As with many early device structures, there are many methods of device-improvement. Ideas for future research to enhance performance of devices fabricated in this thesis are covered in the following section.

7.2 Further Work

As both PbS QD and Ag NW technology continues to develop independently, the improvements may be integrated and adapted within Ag NW-PbS QD solar cells so as to enhance the device as a whole.

7.2.1 SILVER NANOWIRE FILM IMPROVEMENT

In order to reduce the cost of fabrication, the entire device would be fully solution-processed. A solution-processed Ag NW-polymer substrate was thus attempted by depositing a 10% PVA-H_2O solution on heat-treated Ag NWs on glass. The water evaporated within 24 hours, leaving a transparent PVA film behind. The NWs adhered to the polymer when the PVA film was removed from the glass, resulting in a flexible Ag NW-PVA TC with conductivities equivalent to ITO (Figure 7.1). Although this was a side-project and was not applied to device-fabrication, continuation of this research has the potential to yield highly-flexible Ag NW-PbS QD devices at a lower cost than previously mentioned in this thesis. Additionally, embedding Ag NWs in a polymer has proven to reduce Ag NW film roughness to less than 5nm.[45] Thus an Ag NW-polymer TC would not only reduce the cost of the device but could enhance device performance by reduced short-circuiting.

Currently, the 2 hour sintering step is a hurdle for high-throughput TC fabrication. A photonic curing process, such as a PulseForge® system, can eliminate sinter steps to improve NW conductivity on a low-temperature polymer substrate. This process would allow for direct fusion of Ag NWs on a polymer substrate and could also increase throughput of Ag NW TCs when applied as a roll-to-roll process.[113,114]

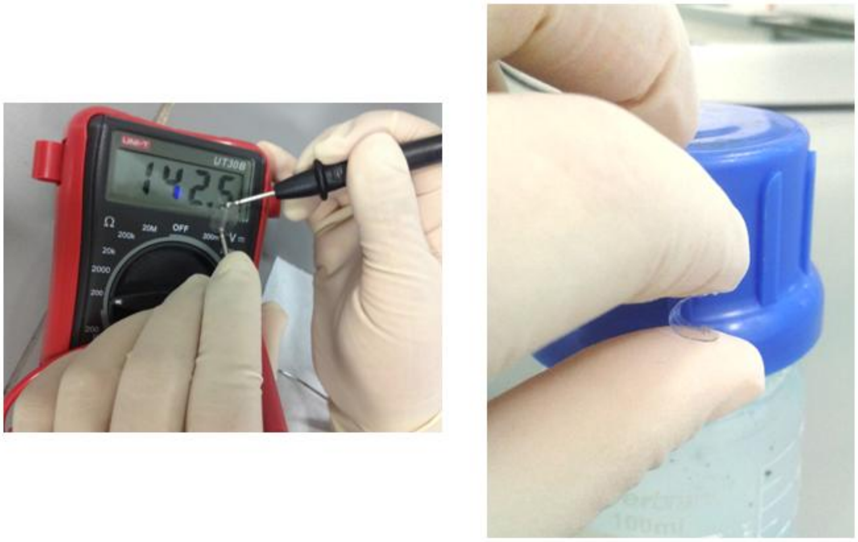

Figure 7.1: Proof of device-quality flexible Ag NW TC

Longer Ag NWs were successfully synthesized using successive multistep growth (SMG). This involves removal of shorter NWs and further addition of Ag NW precursors during synthesis.[33] However, solar cells in this thesis were not fabricated using SMG NWs due to highly variable NW diameter size and increased likelihood of NW agglomeration due to higher concentrations of PVP during NW synthesis. If these issues could be overcome, SMG Ag NWs could make higher transparency TCs with fewer resistive Ag NW junctions for higher quality QD solar cells.

Although light transmission is increased with a low-density NW film of longer, thinner NWs, this would result in a larger area of exposed non-conductive substrate which could not collect generated charge carriers.[42] This may call for an increase in hole mean free path within the PEDOT:PSS layer to avoid recombination before uptake at the PEDOT:PSS-NW interface. Doping PEDOT:PSS, resulting in a higher conductive film, may be one method of resolving this issue to enhance device performance [115]. The PEDOT:PSS layer should also be varied to a greater degree to balance greater smoothing effects with thicker films with reduced charge mobility.[95]

7.2.2 QUANTUM DOT LAYER IMPROVEMENT

As observed in the last section of Chapter 6, J_{sc} and PCE values were relatively invariable as a function of PbS thickness. It was proposed that this is caused by increased junction area, allowing for charge collection at depths not typical of standard ITO-PbS QD cells. Future research should further increase PbS film thickness to determine the optimal PbS thickness before J_{sc} decreases due to significant exciton generation beyond an exciton diffusion length of the depletion region.[71]

PbS QD synthesis was outside the scope of this thesis, therefore a well-established, reproducible PbS synthesis procedure was chosen to provide QDs for this thesis.[57] However, recent advancements in QD synthesis methods should be incorporated in this device structure to enhance cell performance. Currently, poor environmental stability is a major hurdle for QD devices to overcome for commercialization. However, successful synthesis and testing of PbS-CdS core-shell QDs has significantly increased QD photo and thermal stability by greater surface passivation.[116] Combining this QD synthesis with an optimised ligand exchange could yield significantly more stable devices than those tested in this thesis.

As noted in Chapter 2, ligands play a significant role in charge-extraction rates, cracking and device performance.[65] Because this thesis focused on the fabrication and processing of a new solar cell structure, very little time was spent on ligand selection. Future studies should investigate the relationship between device performance and ligand selection for this device structure, including the organic ligands listed in 2.3.3 and metal chalcogenide complexes which have recently been found to enhance charge carrier extraction.[117,118]

REFERENCES

1 Chapin, D., Fuller, C. & Pearson, G. A new silicon p-n junction photocell for converting solar radiation into electrical power. *Journal of Applied Physics* **25**, 676-677 (1954).

2 Goetzberger, A., Luther, J. & Willeke, G. Solar cells: past, present, future. *Solar Energy Materials and Solar Cells* **74**, 1-11 (2002).

3 Crabtree, G. W. & Lewis, N. S. Solar energy conversion. *Physics today* **60**, 37-42 (2007).

4 Fthenakis, V. M., Kim, H. C. & Alsema, E. Emissions from photovoltaic life cycles. *Environmental science & technology* **42**, 2168-2174 (2008).

5 Bazilian, M. *et al.* Re-considering the economics of photovoltaic power. *Renewable Energy* **53**, 329-338 (2013).

6 Green, M. A. Thin-film solar cells: review of materials, technologies and commercial status. *Journal of Materials Science: Materials in Electronics* **18**, 15-19 (2007).

7 Shah, A., Torres, P., Tscharner, R., Wyrsch, N. & Keppner, H. Photovoltaic technology: the case for thin-film solar cells. *Science* **285**, 692-698 (1999).

8 Pagliaro, M., Ciriminna, R. & Palmisano, G. Flexible solar cells. *ChemSusChem* **1**, 880-891 (2008).

9 Hecht, D. S., Hu, L. & Irvin, G. Emerging transparent electrodes based on thin films of carbon nanotubes, graphene, and metallic nanostructures. *Advanced Materials* **23**, 1482-1513 (2011).

10 Sargent, E. H. Colloidal quantum dot solar cells. *Nature Photonics* **6**, 133-135 (2012).

11 Wiley, B., Sun, Y. & Xia, Y. Synthesis of Silver Nanostructures with Controlled Shapes and Properties. *Accounts of Chemical Research* **40**, 1067-1076, doi:10.1021/ar7000974 (2007).

12 Gordon, R. G. Criteria for Choosing Transparent Conductors. *MRS Bulletin,* 52-57 (2000).

13 NanoMarkets. (2011).

14 Hu, L., Kim, H. S., Lee, J. Y., Peumans, P. & Cui, Y. Scalable coating and properties of transparent, flexible, silver nanowire electrodes. *ACS nano* **4**, 2955-2963 (2010).

15 K.L. Chopra, S. M. a. D. K. P. Transparent Conductors- An Overview. *Thin Solid Films* **102**, 1-46 (1983).

16 Lee, J.-Y., Connor, S. T., Cui, Y. & Peumans, P. Solution-processed metal nanowire mesh transparent electrodes. *Nano letters* **8**, 689-692 (2008).

17 Hugh D. Young, R. A. F., Lewis Ford. *Sears and Zemansky's University Physics*. 12 edn, (Addison-Wesley, 2007).

18 Lewis, B. G. & Paine, D. C. and Processing of Transparent Conducting Oxides. *MRS Bulletin*, 23 (2000).

19 De, S. *et al.* Silver nanowire networks as flexible, transparent, conducting films: extremely high DC to optical conductivity ratios. *ACS nano* **3**, 1767-1774 (2009).

20 Kapilevich, I. & Skumanich, A. in *Photovoltaic Specialists Conference (PVSC), 2009 34th IEEE.* 002055-002060.

21 Survey, U. S. G. (ed U.S. Department of the Interior) 198 (Reston, 2012).

22 Hu, L., Hecht, D. & Grüner, G. Percolation in transparent and conducting carbon nanotube networks. *Nano letters* **4**, 2513-2517 (2004).

23 Baughman, R. H., Zakhidov, A. A. & de Heer, W. A. Carbon nanotubes--the route toward applications. *Science* **297**, 787-792 (2002).

24 Kim, K. S. *et al.* Large-scale pattern growth of graphene films for stretchable transparent electrodes. *Nature* **457**, 706-710 (2009).

25 OConnor, B., Haughn, C., An, K.-H., Pipe, K. P. & Shtein, M. Transparent and conductive electrodes based on unpatterned, thin metal films. *Applied Physics Letters* **93**, 223304-223304-223303 (2008).

26 Zhu, R. *et al.* Fused silver nanowires with metal oxide nanoparticles and organic polymers for highly transparent conductors. *ACS nano* **5**, 9877-9882 (2011).

27 Hu, J., Odom, T. W. & Lieber, C. M. Chemistry and physics in one dimension: synthesis and properties of nanowires and nanotubes. *Accounts of Chemical Research* **32**, 435-445 (1999).

28 Lee, J. H., Lee, P., Lee, D., Lee, S. S. & Ko, S. H. Large-Scale Synthesis and Characterization of Very Long Silver Nanowires via Successive Multistep Growth. *Crystal Growth & Design* **12**, 5598-5605, doi:10.1021/cg301119d (2012).

29 Sun, Y., Gates, B., Mayers, B. & Xia, Y. Crystalline silver nanowires by soft solution processing. *Nano letters* **2**, 165-168 (2002).

30 Madaria, A. R., Kumar, A., Ishikawa, F. N. & Zhou, C. Uniform, highly conductive, and patterned transparent films of a percolating silver nanowire network on rigid and flexible substrates using a dry transfer technique. *Nano research* **3**, 564-573 (2010).

31 Pike, G. & Seager, C. Percolation and conductivity: A computer study. I. *Physical review B* **10**, 1421 (1974).

32 Xia, Y., Xiong, Y., Lim, B. & Skrabalak, S. E. Shape-Controlled Synthesis of Metal Nanocrystals: Simple Chemistry Meets Complex Physics? *Angewandte Chemie International Edition* **48**, 60-103 (2008).

33 Lee, J. *et al.* Very Long Ag Nanowire Synthesis and Its Application for a Highly Transparent, Conductive and Flexible Metal Electrode Touch Panel. *Nanoscale* (2012).

34 Lu, X., Rycenga, M., Skrabalak, S. E., Wiley, B. & Xia, Y. Chemical synthesis of novel plasmonic nanoparticles. *Annual review of physical chemistry* **60**, 167-192 (2009).

35 Chen, C. *et al.* Study on the synthesis of silver nanowires with adjustable diameters through the polyol process. *Nanotechnology* **17**, 3933 (2006).

36 Korte, K. E., Skrabalak, S. E. & Xia, Y. Rapid synthesis of silver nanowires through a CuCl-or CuCl2-mediated polyol process. *J. Mater. Chem.* **18**, 437-441 (2007).

37 Pietrobon, B., McEachran, M. & Kitaev, V. Synthesis of size-controlled faceted pentagonal silver nanorods with tunable plasmonic properties and self-assembly of these nanorods. *ACS nano* **3**, 21-26 (2008).

38 Rycenga, M. *et al.* Controlling the synthesis and assembly of silver nanostructures for plasmonic applications. *Chemical Reviews-Columbus* **111**, 3669 (2011).

39 Nelson, M. *Metal Nanowire-Organic Composite for Transparent Conductors* M.Eng. thesis, University of Oxford, (2012).

40 Scardaci, V., Coull, R., Lyons, P. E., Rickard, D. & Coleman, J. N. Spray Deposition of Highly Transparent, Low-Resistance Networks of Silver Nanowires over Large Areas. *Small* **7**, 2621-2628 (2011).

41 Lee, J. *et al.* Room-Temperature Nanosoldering of a Very Long Metal Nanowire Network by Conducting-Polymer-Assisted Joining for a Flexible Touch-Panel Application. *Advanced Functional Materials* (2013).

42 Ajuria, J. *et al.* Insights on the working principles of flexible and efficient ITO-free organic solar cells based on solution processed Ag nanowire electrodes. *Solar Energy Materials and Solar Cells* **102**, 148-152, doi:http://dx.doi.org/10.1016/j.solmat.2012.03.009 (2012).

43 Coskun, S., Ates, E. S. & Unalan, H. E. Optimization of silver nanowire networks for polymer light emitting diode electrodes. *Nanotechnology* **24**, 125202 (2013).

44 Madaria, A. R., Kumar, A. & Zhou, C. Large scale, highly conductive and patterned transparent films of silver nanowires on arbitrary substrates and their application in touch screens. *Nanotechnology* **22**, 245201 (2011).

45 Yu, Z. *et al.* Highly Flexible Silver Nanowire Electrodes for Shape-Memory Polymer Light-Emitting Diodes. *Advanced Materials* **23**, 664-668 (2011).

46 Morgenstern, F. S. *et al.* Ag-nanowire films coated with ZnO nanoparticles as a transparent electrode for solar cells. *Applied physics letters* **99**, 183307-183307-183303 (2011).

47 Hardin, B. E. *et al.* Laminating solution-processed silver nanowire mesh electrodes onto solid-state dye-sensitized solar cells. *Organic Electronics* **12**, 875-879 (2011).

48 Jørgensen, M., Norrman, K. & Krebs, F. C. Stability/degradation of polymer solar cells. *Solar Energy Materials and Solar Cells* **92**, 686-714 (2008).

49 Nelson, J. *The Physics of Solar Cells*. (Imperial College Press, 2010).

50 Freedman, H. D. Y. a. R. A. *University Physics*. Vol. 2 (Addison-Wesley, 2007).

51 Kasap, S. O. *Principles of Electronic Materials and Devices*. 3rd edn, (McGraw-Hill Companies, 2006).

52 Green, M. A. *Solar Cells: Operating Principles, Technology and System Applications*. (Prentice-Hall, 1982).

53 Pysch, D., Mette, A. & Glunz, S. A review and comparison of different methods to determine the series resistance of solar cells. *Solar Energy Materials and Solar Cells* **91**, 1698-1706 (2007).

54 Ishibashi, K.-i., Kimura, Y. & Niwano, M. An extensively valid and stable method for derivation of all parameters of a solar cell from a single current-voltage characteristic. *Journal of applied physics* **103**, 094507-094507-094506 (2008).

55 Murray, C., Kagan, C. & Bawendi, M. Synthesis and characterization of monodisperse nanocrystals and close-packed nanocrystal assemblies. *Annual Review of Materials Science* **30**, 545-610 (2000).

56 Leutwyler, W. K., Bürgi, S. L. & Burgl, H. Semiconductor clusters, nanocrystals, and quantum dots. *Science* **271**, 933 (1996).

57 Hines, M. A. & Scholes, G. D. Colloidal PbS nanocrystals with size-tunable near-infrared emission: observation of post-synthesis self-narrowing of the particle size distribution. *Advanced Materials* **15**, 1844-1849 (2003).

58 Nozik, A. *et al.* Semiconductor quantum dots and quantum dot arrays and applications of multiple exciton generation to third-generation photovoltaic solar cells. *Chemical reviews* **110**, 6873 (2010).

59 Murray, C., Norris, D. & Bawendi, M. G. Synthesis and characterization of nearly monodisperse CdE (E= sulfur, selenium, tellurium) semiconductor nanocrystallites. *Journal of the American Chemical Society* **115**, 8706-8715 (1993).

60 Yu, W. W., Falkner, J. C., Shih, B. S. & Colvin, V. L. Preparation and characterization of monodisperse PbSe semiconductor nanocrystals in a noncoordinating solvent. *Chemistry of Materials* **16**, 3318-3322 (2004).

61 Ahrenkiel, S. *et al.* Synthesis and characterization of colloidal InP quantum rods. *Nano Letters* **3**, 833-837 (2003).

62 Guzelian, A., Banin, U., Kadavanich, A., Peng, X. & Alivisatos, A. Colloidal chemical synthesis and characterization of InAs nanocrystal quantum dots. *Applied Physics Letters* **69**, 1432-1434 (1996).

63 Lee, J.-W. *et al.* Quantum-Dot-Sensitized Solar Cell with Unprecedentedly High Photocurrent. *Scientific reports* **3** (2013).

64 Choi, J. J. *et al.* PbSe nanocrystal excitonic solar cells. *Nano letters* **9**, 3749-3755 (2009).

65 Hanrath, T. Colloidal nanocrystal quantum dot assemblies as artificial solids. *Journal of Vacuum Science & Technology A: Vacuum, Surfaces, and Films* **30**, 030802-030802-030828 (2012).

66 Tang, J. *et al.* Colloidal-quantum-dot photovoltaics using atomic-ligand passivation. *Nature materials* **10**, 765-771 (2011).

67 Wang, X. *et al.* Tandem colloidal quantum dot solar cells employing a graded recombination layer. *Nature Photonics* **5**, 480-484 (2011).

68 Zhai, G. *et al.* Air stability of TiO2/PbS colloidal nanoparticle solar cells and its impact on power efficiency. *Applied Physics Letters* **99**, 063512 (2011).

69 Jeong, K. S. *et al.* Enhanced mobility-lifetime products in PbS colloidal quantum dot photovoltaics. *Acs Nano* **6**, 89-99 (2011).

70 Luther, J. M. *et al.* Stability assessment on a 3% bilayer PbS/ZnO quantum dot heterojunction solar cell. *Advanced Materials* **22**, 3704-3707 (2010).

71 Willis, S. M., Cheng, C., Assender, H. E. & Watt, A. A. The transitional heterojunction behavior of PbS/ZnO colloidal quantum dot solar cells. *Nano Letters* **12**, 1522-1526 (2012).

72 Pattantyus-Abraham, A. G. *et al.* Depleted-heterojunction colloidal quantum dot solar cells. *ACS nano* **4**, 3374-3380 (2010).

73 Nozik, A. Quantum dot solar cells. *Physica E: Low-dimensional Systems and Nanostructures* **14**, 115-120 (2002).

74 Hossain, M. A., Koh, Z. Y. & Wang, Q. PbS/CdS-sensitized mesoscopic SnO2 solar cells for enhanced infrared light harnessing. *Physical Chemistry Chemical Physics* **14**, 7367-7374 (2012).

75 Wang, P., Wang, L., Ma, B., Li, B. & Qiu, Y. TiO2 surface modification and characterization with nanosized PbS in dye-sensitized solar cells. *The Journal of Physical Chemistry B* **110**, 14406-14409 (2006).

76 Gao, J. *et al.* Quantum Dot Size Dependent J− V Characteristics in Heterojunction ZnO/PbS Quantum Dot Solar Cells. *Nano letters* **11**, 1002-1008 (2011).

77 Lao, J. Y., Wen, J. G. & Ren, Z. F. Hierarchical ZnO nanostructures. *Nano letters* **2**, 1287-1291 (2002).

78 Choi, J. J. *et al.* Photogenerated exciton dissociation in highly coupled lead salt nanocrystal assemblies. *Nano Letters* **10**, 1805-1811 (2010).

79 Barkhouse, D. A. R. *et al.* Depleted bulk heterojunction colloidal quantum dot photovoltaics. *Advanced Materials* **23**, 3134-3138 (2011).

80 Gregg, B. A. Excitonic solar cells. *The Journal of Physical Chemistry B* **107**, 4688-4698 (2003).

81 Johnston, K. W. *et al.* Schottky-quantum dot photovoltaics for efficient infrared power conversion. *Applied Physics Letters* **92**, 151115-151115-151113 (2008).

82 Kramer, I. J. & Sargent, E. H. Colloidal quantum dot photovoltaics: a path forward. *Acs Nano* **5**, 8506-8514 (2011).

83 Bouclé, J. & Ackermann, J. Solid-state dye-sensitized and bulk heterojunction solar cells using TiO2 and ZnO nanostructures: recent progress and new concepts at the borderline. *Polymer International* **61**, 355-373 (2012).

84 Leschkies, K. S., Jacobs, A. G., Norris, D. J. & Aydil, E. S. Nanowire-quantum-dot solar cells and the influence of nanowire length on the charge collection efficiency. *Applied Physics Letters* **95**, 193103-193103-193103 (2009).

85 Maraghechi, P. *et al.* The Donor-Supply Electrode Enhances Performance in Colloidal Quantum Dot Solar Cells. *Acs Nano* (2013).

86 Skrabalak, S. E., Wiley, B. J., Kim, M., Formo, E. V. & Xia, Y. On the polyol synthesis of silver nanostructures: glycolaldehyde as a reducing agent. *Nano letters* **8**, 2077-2081 (2008).

87 Pacholski, C., Kornowski, A. & Weller, H. Self-Assembly of ZnO: From Nanodots to Nanorods. *Angewandte Chemie International Edition* **41**, 1188-1191 (2002).

88 Group, D. I. V. M. (2002).

89 Smits, F. Measurement of sheet resistivities with the four-point probe. *Bell Syst. Tech. J* **37**, 711-718 (1958).

90 Jacquez, J. A. & Kuppenheim, H. F. Theory of the integrating sphere. *JOSA* **45**, 460-466 (1955).

91 Finkel, M. W. Integrating sphere theory. *Optics Communications* **2**, 25-28 (1970).

92 ADE Phase Shift Technology, I. (Tuscon, 2002).

93 Verbakel, F., Meskers, S. C. & Janssen, R. A. Electronic memory effects in diodes from a zinc oxide nanoparticle-polystyrene hybrid material. *Applied Physics Letters* **89**, 102103-102103-102103 (2006).

94 Korte, K. E., Skrabalak, S. E. & Xia, Y. Rapid synthesis of silver nanowires through a CuCl- or CuCl2-mediated polyol process. *Journal of Materials Chemistry* **18**, 437-441 (2008).

95 Yang, L. *et al.* Solution-processed flexible polymer solar cells with silver nanowire electrodes. *ACS applied materials & interfaces* **3**, 4075-4084 (2011).

96 Ghosh, R., Basak, D. & Fujihara, S. Effect of substrate-induced strain on the structural, electrical, and optical properties of polycrystalline< equation>< font face='verdana'> ZnO</equation> thin films. *Journal of applied physics* **96**, 2689-2692 (2004).

97 De, S., King, P. J., Lyons, P. E., Khan, U. & Coleman, J. N. Size effects and the problem with percolation in nanostructured transparent conductors. *ACS nano* **4**, 7064-7072 (2010).

98 Granqvist, C. & Hultåker, A. Transparent and conducting ITO films: new developments and applications. *Thin Solid Films* **411**, 1-5 (2002).

99 Sanders, A. W. *et al.* Observation of plasmon propagation, redirection, and fan-out in silver nanowires. *Nano letters* **6**, 1822-1826 (2006).

100 Kumar Barik, U., Srinivasan, S., Nagendra, C. & Subrahmanyam, A. Electrical and optical properties of reactive DC magnetron sputtered silver oxide thin films: role of oxygen. *Thin Solid Films* **429**, 129-134 (2003).

101 Tjeng, L. *et al.* Electronic structure of Ag_ {2} O. *Physical Review B* **41**, 3190 (1990).

102 Xu, C., Sun, X., Zhang, X., Ke, L. & Chua, S. Photoluminescent properties of copper-doped zinc oxide nanowires. *Nanotechnology* **15**, 856 (2004).

103 Willis, S. *Advanced Optoelectronic Characterisation of Solar Cells* D.Phil thesis, University of Oxford, (2011).

104 Liston, E. M. Plasma treatment for improved bonding: a review. *The Journal of Adhesion* **30**, 199-218 (1989).

105 Khaligh, H. H. & Goldthorpe, I. A. Failure of silver nanowire transparent electrodes under current flow. *Nanoscale research letters* **8**, 1-6 (2013).

106 Natsume, Y. & Sakata, H. Zinc oxide films prepared by sol-gel spin-coating. *Thin Solid Films* **372**, 30-36 (2000).

107 Kang, H. S. *et al.* Structural, electrical, and optical properties of< equation> p</equation>-type ZnO thin films with Ag dopant. *Applied Physics Letters* **88**, 202108-202108-202103 (2006).

108 Lin, T.-H., Chen, T.-T., Cheng, C.-L., Lin, H.-Y. & Chen, Y.-F. Selectively enhanced band gap emission in ZnO/Ag< sub> 2</sub> O nanocomposites. *Optics Express* **17**, 4342-4347 (2009).

109 Hosono, E., Fujihara, S. & Kimura, T. Fabrication and electrical properties of micro/nanoporous ZnO∶ Al films. *J. Mater. Chem.* **14**, 881-886 (2004).

110 Schmidt, M., Masson, A. & Brechignac, C. Oxygen and silver clusters: Transition from chemisorption to oxidation. *Physical review letters* **91**, 243401 (2003).

111 Tvarusko, A. The Electric Resistivity of AgO. *Journal of The Electrochemical Society* **115**, 1105-1110 (1968).

112 Tang, J. *et al.* Schottky quantum dot solar cells stable in air under solar illumination. *Advanced Materials* **22**, 1398-1402 (2010).

113 West, J., Carter, M., Smith, S. & Sears, J. Photonic Sintering of Silver Nanoparticles: Comparison of Experiment and Theory.

114 NovaCentrix. (Austin, Texas, 2012).

115 Crispin, X. *et al.* The origin of the high conductivity of poly (3, 4-ethylenedioxythiophene)-poly (styrenesulfonate)(PEDOT-PSS) plastic electrodes. *Chemistry of Materials* **18**, 4354-4360 (2006).

116 Zhao, H., Chaker, M., Wu, N. & Ma, D. Towards controlled synthesis and better understanding of highly luminescent PbS/CdS core/shell quantum dots. *Journal of Materials Chemistry* **21**, 8898-8904 (2011).

117 Kovalenko, M. V., Scheele, M. & Talapin, D. V. Colloidal nanocrystals with molecular metal chalcogenide surface ligands. *Science* **324**, 1417-1420 (2009).

118 Podsiadlo, P. *et al.* The role of order, nanocrystal size, and capping ligands in the collective mechanical response of three-dimensional nanocrystal solids. *Journal of the American Chemical Society* **132**, 8953-8960 (2010).